

Excitation Energy Transfer and Delocalization in Trapped-ion Quantum Simulator: A Numerical Study

Senior Thesis submitted in partial fulfillment of the requirements
for the degree of Bachelor of Science in General Physics

Mingjian Zhu*

Department of Physics and Astronomy, Rice University

2023



RICE

*mz40@rice.edu

Abstract

In recent years, Analog Quantum Simulation (AQS) has emerged as a powerful experimental platform for investigating the physics of quantum-many body systems. This thesis presents a numerical study of trapped-ion AQS for future experimental work on Excitation Energy Transport (EET) and anharmonicity induced delocalization in molecular systems. We propose prototype simulator setups by illustrating the exact mapping between the target models and the trapped-ion simulator. We use numerical simulations to guide future experiments. Our numerical results on EET show good agreement with previous research. The contribution of anharmonicity to the delocalization dynamics still requires further investigation. We also identify potential inconsistencies between different signatures of quantum chaos, which could help develop theories in related topics.

Acknowledgement

I would like to express my heartfelt gratitude to the following people who have played a significant role in the completion of my undergraduate study.

First and foremost, I extend my sincerest appreciation to my major advisor, Dr. Guido Pagano, for his unwavering guidance, support for my undergraduate research and PhD application. His expertise, patience, and encouragement have been instrumental in shaping the direction of my research.

I would also like to thank the collaborators of our group, Dr. Han Pu and Diego Fallas, for their invaluable advice and for working together with me on the study of delocalization. Their inputs and insights have been invaluable in advancing my understanding of the subject.

To everyone in our group, Dr. Roman Zhuravel, Visal So, Abhishek Menon, Midhuna Duraisamy Suganthi, and April Sheffield, I extend my gratitude for their help in the lab, feedback on my research, and the stimulating discussions we had. I am grateful to have been a part of such a supportive and collaborative team.

I would like to express my sincere thanks to Dr. Peter Wolynes and Dr. Martin Gruebele for providing expert suggestions and guidance on our research directions. Their support have been crucial in advancing our research.

I would also like to thank my parents for their unwavering support throughout my pursuit of B.S. degree in physics. Their love, encouragement, and belief in me have been my driving force.

Lastly, I would like to express my appreciation to my friends at Rice and in the group chat 吃饱喝足 , who have been a source of joy and motivation during the difficult times. Their unwavering support and enthusiasm have been an essential part of my journey.

Contents

1	Introduction	6
2	Target Models for Simulation	7
2.1	EET in Donor-Acceptor Pair	7
2.2	Anharmonicity induced Quantum Delocalization	8
3	Trapped Ions Systems	9
3.1	Quantum Dynamics of Trapped Ions	9
3.1.1	Classical Harmonic Motion	9
3.1.2	Quantum Hamiltonian	11
3.2	Ion Interaction with Classical Light Field	12
3.2.1	Dipole Approximation	12
3.2.2	Ordinary Interaction Frame	13
4	Mapping to Target Models	15
4.1	Spin-only Operators	15
4.2	Donor-Acceptor Pair System	16
4.3	Anharmonic Phonon Coupling	18
4.4	Anharmonic Spin-phonon System with Two Drives	19
4.5	Anharmonic Spin-phonon system with One Drive	21
4.6	Summary	22
5	Methods	23
5.1	Approximations of Hamiltonian	23
5.2	Quantum Time Evolution	24
5.3	Energy Diagram	24
5.4	Signatures of Quantum Chaos and Delocalization	25
6	Results and Discussion	26
6.1	Donor-Acceptor Pair: Trapped-ion Simulation	26
6.1.1	Hamiltonian under Approximation	26
6.1.2	Numerical results	28
6.1.3	Discussion	30
6.2	Anharmonicity Induced Delocalization	31
6.2.1	Parameter Space and Simulation Procedure	31
6.2.2	Two-drive configuration: Hamiltonian under Approximation	32
6.2.3	Two-drive configuration with one site: Numerical Results	33
6.2.4	Two-drive configuration with multiple Sites: Numerical Results	35
6.2.5	One-drive configuration: Hamiltonian under Approximation	37
6.2.6	One-drive system: Numerical Results	38
6.2.7	Discussion	40
7	Conclusion	41
8	Appendix	41
8.1	Appendix A	41
	1D Equilibrium Position	41
	Tensors in Lagrangian	42

8.2	Appendix B	42
	Derivation of Hamiltonian in ordinary interaction frame	42
	Derivation of Hamiltonian in resonant interaction frame	44
8.3	Appendix C	45
	8.3.1 Thermal state and average phonon number	45
8.4	Appendix D	46
	8.4.1 Relation between Decay rate and Dissipation in EET	46

1 Introduction

Quantum simulation experiments have emerged as a powerful tool for probing the behavior of quantum systems in diverse fields, ranging from condensed matter physics and high-energy physics to atomic physics and quantum chemistry [1]. In Analog Quantum Simulation (AQS), a Hamiltonian and corresponding dissipative environment that exactly map to target natural phenomena will be engineered based on various simulator platforms, including atoms in optical lattice, electron spins in semiconductor quantum dots, trapped-ions, and cavity photons [2]. Rather than being restricted by the fixed properties of a natural system, the engineered simulator Hamiltonian has tunable parameters which are usually controlled by external electromagnetic fields. This enables researchers to explore a significantly wider parameter space, thereby enhancing the scope and efficiency of their investigations. The quantum nature of the simulator helps avoiding the exponential growth of computational resources that a classical computer would require to solve quantum problems. A typical example of AQS is simulating the Hubbard model with atoms in an optical lattice [3].

Trapped-ion systems are considered to be a highly efficient and versatile platform for implementing AQS. A comprehensive review of related techniques can be found in [4]. A common setup involves laser-cooled atomic ions within a vacuum chamber confined by radio-frequency pseudopotentials and manipulated via applied external lasers or microwaves. The intrinsic electronic levels and quantum vibrations of the confined ions serve as an ideal basis for creating many-body spin-phonon (boson) systems. With external optical fields, coherent and dissipative quantum interactions of desired form and magnitude can be generated in these systems. Trapped-ion systems enable a large number of ionic qubits under control and well controlled interactions. The long coherence time of qubits (on the order of minutes [5]) also allows the creation of quantum states with high fidelity. Such advantages make the trapped-ion platform an ideal experimental framework for exploring fundamental phenomena in many-body quantum physics. In this theoretical project, we examine the potential of applying trapped-ion AQS to solve problems in molecular chemical physics, specifically focusing on energy transfer and quantum localization in photosynthetic systems.

Photosynthesis is a fundamental process for organisms to harvest and store solar energy. Photons are captured and converted into electronic excitation by antenna complexes. The energy captured is then transferred into the reaction center for storage under the interaction with an external environment through an Excitation Energy Transfer (EET) process [6, 7]. Depending on the strength of exciton coupling V and environmental dissipation Γ , EET can be categorized into incoherent ($V \ll \Gamma$) regime, coherent ($V \gg \Gamma$) regime, and an intermediate regime.

Numerous quantum physics and biochemistry research efforts have been conducted to develop theories about EET. A recent in-depth review of related topics can be found in [8]. In general, the corresponding quantum system is described in displaced harmonic oscillator formalism as a spin system coupled by molecular phonon modes [9]. Transfer mechanism in incoherent regime can be well explained quantitatively using Forster and generalized Forster resonance energy transfer theory based on equilibrium Fermi Golden Rule approach [10, 11]. Physics in the coherent regime can be modeled by Redfield Theory based on open quantum system dynamics which describes the environment as an external heat bath with correlation functions determined by spectral density function $J(\omega)$ [12, 13]. Various approaches have also been employed to handle the intermediate regime, including coherent modified Redfield Theory and hierarchical equation of motion formalism [14, 15].

Many realms of EET still remain unexplored, especially in the intermediate regime where most

realistic photosynthetic processes takes place. Experimental and numerical research has shown that quantum coherence and molecular vibrational modes have important effects on the efficiency of EET [16, 17, 18, 19]. Evidence has also been found for the contribution of entanglement to EET [20, 21].

On the other hand, spin-phonon systems in photosynthetic processes may serve as useful models for studying quantum delocalization, chaotic behavior in which a closed quantum system thermally equilibrates under its own dynamics. The spread of quantum entanglement will effectively remove the system’s memory of its initial local properties such that in long-time thermal equilibrium the system can be characterized by thermodynamic quantities [22]. Numerical studies on photosynthetic systems have identified transitions from coherent organized behavior to chaotic delocalization phenomenon, induced by quantum transport networks consisting of vibrational states coupled with Fermi-resonance anharmonicity [23, 24, 25].

More experimental research is required to investigate the validity of theories and discover new phenomena in the above fields. Related quantum simulation experiments have been conducted using semiconductor quantum dots [26, 27], Rydberg Atoms [28], and trapped-ion system [29, 30]. In this thesis, We demonstrate the feasibility of reconstructing target Hamiltonians for vibration-environment assisted EET and anharmonicity induced quantum delocalization in trapped-ion systems from a theoretical perspective. We propose several setups of prototype simulators for preliminary AQS experiments. Since the quantum complexity of these setups is still within the capability of a classical computer, we also use various numerical methods to simulate experimental results. Overall, this project lays the theoretical groundwork and serves as a pilot study for a series of forthcoming experimental investigations. Its general aim is to determine the appropriate parameter ranges and provide valuable insights into potential outcomes.

In Section 2, we discuss the quantum models for target phenomena of interest. In sections 3 and 4 we review the physics of trapped-ion systems interacting with external light fields and illustrate how the target Hamiltonian/dissipative environment can be generated. We discuss the numerical methods and approximations that will be used to study the quantum dynamics of the simulator in Section 5. We present the results of the numerical simulations followed by a discussion of their significance in Section 6. Conclusions are presented in Section 7.

2 Target Models for Simulation

In this section we discuss the Hamiltonian of each target model in details¹.

2.1 EET in Donor-Acceptor Pair

The first model of interest for vibrational-environment assisted EET is consisted of a pair of donor and acceptor molecular sites coupled to a shared set of n intermolecular modes. The system weakly interacts with an external heat bath, or reservoir, at temperature T . The electronic degree of freedom of each site is considered as a spin 1/2 space with a ground state and an excited state. The Hamiltonian of the system can be described by [18, 26]:

$$\hat{H} = \sum_{i=1}^2 E_i \hat{\sigma}_z^i + J_{12} (\hat{\sigma}_1^+ \hat{\sigma}_2^- + h.c.) + \sum_{m=1}^n \omega_m \hat{a}_m^\dagger \hat{a}_m + \sum_{i=1}^2 \sum_{m=1}^n \lambda_{im} (\hat{a}_m^\dagger + \hat{a}_m) \hat{\sigma}_z^i. \quad (2.1)$$

¹In this thesis we use energy scale of \hbar for convenience by setting $\hbar = 1$ in all Hamiltonians.

E_i is the energy difference between the electronic excited state and ground state for site i . J_{12} is the Forster exciton coupling coefficient between 2 sites. The spin space ladder operators are defined as:

$$\hat{\sigma}^{\pm} = (\hat{\sigma}_x \pm i\hat{\sigma}_y)/2, \quad (2.2)$$

where $\hat{a}_m^{\dagger}, \hat{a}_m$ are the phonon ladder operators for the m th phonon space. λ_{im} is the spin-phonon coupling strength between site i and vibrational mode m .

The model assumes a sufficiently weak incoherent phonon interaction between the external reservoir and the spin-phonon system. Under Born-Markov approximation[31], this interaction can be described by a Lindbladian super-operator:

$$\hat{L}(\hat{\rho}) = \sum_m \Gamma_m^- \left(\hat{a}_m \hat{\rho} \hat{a}_m^{\dagger} - \frac{1}{2} [\hat{a}_m^{\dagger} \hat{a}_m, \hat{\rho}] \right) + \Gamma_m^+ \left(\hat{a}_m^{\dagger} \hat{\rho} \hat{a}_m - \frac{1}{2} [\hat{a}_m \hat{a}_m^{\dagger}, \hat{\rho}] \right). \quad (2.3)$$

Dissipation rates Γ_m^-, Γ_m^+ describes how fast vibrational mode m loses/gains one phonon excitation under the effect of thermal reservoir. The exact value is determined by the property of reservoir [19]. More details on the Lindbladian super-operator \hat{L} will be discussed in section 4.5.

The electronic EET phenomenon is described by the dynamics from a $|\uparrow\downarrow\rangle$ spin state to $|\downarrow\uparrow\rangle$, in which the excited electron is transferred from site 1(donor) to the site 2 (acceptor). The donor-acceptor pair can be effectively reduced to a system of 1 site. Consider the spin operators in product space $|00\rangle, |10\rangle, |01\rangle, |11\rangle$ with convention $|0\rangle \equiv |\uparrow\rangle, |1\rangle \equiv |\downarrow\rangle$

$$\begin{aligned} & A_1 \sigma_z^1 + A_2 \sigma_z^2 \\ &= (A_1 + A_2)(|00\rangle\langle 00| - |11\rangle\langle 11|) + (A_1 - A_2)(|01\rangle\langle 01| - |10\rangle\langle 10|), \\ & J_{12}(\hat{\sigma}_1^+ \hat{\sigma}_2^- + h.c.) = J_{12}(|01\rangle\langle 10| + |01\rangle\langle 10|). \end{aligned} \quad (2.4)$$

The terms $(|00\rangle\langle 00|, |11\rangle\langle 11|)$ have no effect on initial state $|01\rangle$. The effective spin space of the system is spanned by $|0\rangle \equiv |01\rangle, |1\rangle \equiv |10\rangle$. In this new basis the total interaction Hamiltonian becomes:

$$\hat{H}' = \frac{\Delta E}{2} \hat{\sigma}_z + V \hat{\sigma}_x + \sum_{m=1}^n \omega_m \hat{a}_m^{\dagger} \hat{a}_m + \sum_{m=1}^N g_m (\hat{a}_m^{\dagger} + \hat{a}_m) \hat{\sigma}_z. \quad (2.5)$$

These new coefficients maps to parameters in the two-site system following:

$$V = J_{12}, g_m = \lambda_{1m} - \lambda_{2m}, \Delta E = 2(E_1 - E_2). \quad (2.6)$$

The one-site system coupled to a single mode has been well studied in [30] and it is easier to realize experimentally compared to the two-site system.

2.2 Anharmonicity induced Quantum Delocalization

The second model to study is a closed quantum system based on the one-site model for EET with anharmonic coupling between different modes [25]:

$$\hat{H} = \frac{\Delta E}{2} \hat{\sigma}_z + V \hat{\sigma}_x + \sum_{\alpha} \sum_{m=1}^n \omega_m (\hat{a}_m^{\alpha})^{\dagger} \hat{a}_m^{\alpha} + \sum_{\alpha} \sum_{m=1}^n g_{\alpha m} ((\hat{a}_m^{\alpha})^{\dagger} + \hat{a}_m^{\alpha}) \hat{\sigma}_z + \sum_m \prod_{\alpha} \Theta_m (\hat{a}_{\alpha}^{m+})^{\dagger} \hat{a}_{\alpha}^{m-}. \quad (2.7)$$

The last term represents the anharmonic coupling where \hat{a}_m^{α} is the phonon operator for vibrational mode m at degree of freedom α . These modes may come from intermolecular vibrations in a

complicated configuration. The anharmonicity is assumed to be dominated by Fermi resonance (cubic) terms in form $\hat{a}^\dagger \hat{b} \hat{b}$, where \hat{a}, \hat{b} are ladder operators for two distinctive phonon spaces. Another closed system of similar format involves an extended spin space of three sites:

$$\hat{H} = \sum_{i=1}^2 \frac{\Delta E_i}{2} \hat{\sigma}_i^z + \sum_{i=1}^3 V_i \hat{\sigma}_i^x + \sum_{m=1}^n \omega_m \hat{a}_m^\dagger \hat{a}_m + \sum_{i=1}^3 \sum_{m=1}^N g_{im} (\hat{a}_m^\dagger + \hat{a}_m) \hat{\sigma}_i^z + \sum_m \prod_{\alpha} \Theta_m (\hat{b}_{\alpha}^{m+})^\dagger \hat{b}_{\alpha}^{m-}. \quad (2.8)$$

3 Trapped Ions Systems

3.1 Quantum Dynamics of Trapped Ions

In this section we review some important results about basic properties of an ion trap [32]. The parameters to be introduced are essential for the derivations in the next few sections.

3.1.1 Classical Harmonic Motion

A trapped-ion chain can be confined in a linear RF trap [33], where the equilibrium positions are determined by the interplay of Coulomb interaction and harmonic trapping potentials [34]. Let us set up the coordinate system as shown in Figure 1. By setting the voltages on the trap electrodes in the appropriate way, the harmonic frequency of the potential can be set to $\omega_x = \omega_y > \omega_z$ for confinement in x, y, z directions. ω_x, ω_y are assumed to be sufficiently larger than ω_z such that the ions form a 1D chain along \hat{z} axis in stable equilibrium. (the exact condition for the 1D chain will be discussed afterwards) With the position coordinates defined in Figure 1, the mass of ion being M and the charge carried being Q , the Lagrangian of the N -ion system can be written using the equilibrium position \bar{x}_{ni} and displacement from the equilibrium ϵ_{ni} :

$$L = T - V = \frac{M}{2} \sum_{n=1}^N \sum_{i=1}^3 \dot{\epsilon}_{ni}^2 - \frac{M}{2} \sum_{n=1}^N \sum_{i=1}^3 \omega_i^2 (\bar{x}_{ni} + \epsilon_{ni})^2 - \frac{1}{2} \frac{Q^2}{4\pi\epsilon_0} \sum_{n \neq m}^N \left[\sum_{i=1}^3 (\bar{x}_{ni} + \epsilon_{ni} - \bar{x}_{mi} - \epsilon_{mi})^2 \right]^{-\frac{1}{2}}. \quad (3.1)$$

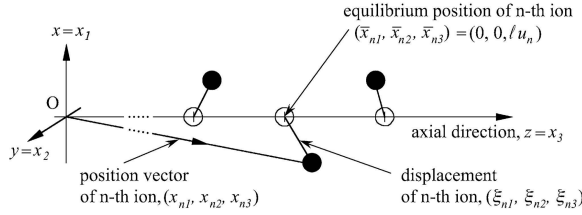


Figure 1: Definition of coordinates for ions confined in a stable configuration. x_{ni} is the position coordinate of ion n in direction i , with $i = 1, 2, 3$ for x, y, z directions, respectively. The equilibrium position and displacement from equilibrium are labeled as \bar{x}_{ni} , ϵ_{ni} , respectively.

Under an order-3 Taylor expansion assuming $\epsilon_{ni} \rightarrow 0$, L can be transformed into a combination of quadratic terms and non-quadratic terms:

$$L \rightarrow L_z + L_{xy} + L_{ah} \quad (3.2)$$

L_z and L_{xy} describe motion due to the harmonic part of the potential in axial and radial directions, respectively.

$$\begin{aligned} L_z &= \frac{M}{2} \left[\sum_{n=1}^N \dot{\epsilon}_{n3}^2 - \omega_3^2 \sum_{m,n=1}^N A_{mn} \epsilon_{m3} \epsilon_{n3} \right] \\ L_{xy} &= \frac{M}{2} \sum_{i=1}^2 \left[\sum_{n=1}^N \dot{\epsilon}_{ni}^2 - \omega_3^2 \sum_{m,n=1}^N B_{mn} \epsilon_{mi} \epsilon_{ni} \right]. \end{aligned} \quad (3.3)$$

The elastic tensors A, B are related by:

$$B_{mn} = \left(\frac{\omega_x^2}{\omega_z^2} + \frac{1}{2} \right) \delta_{mn} - \frac{1}{2} A_{mn}. \quad (3.4)$$

The exact expression of A is given in Appendix 8.1, A only depends on the axial confining frequency ω_z while B depends on both axial and radial frequencies. Since the confining frequencies are the same in \hat{x}, \hat{y} directions, the harmonic Lagrangian for these two degrees of freedom will also take the same form (described by the same elastic tensor B). It is then sufficient to solve the dynamics in either direction. We label this direction as radial in the following derivations.

It can be shown that A is always positive definite. B , however, is positive definite if and only if the assumption of 1-d equilibrium holds. The critical condition for this case is determined by the trap confining frequencies:

$$\alpha = \omega_z^2 / \omega_x^2 < 2 / (\mu_N - 1), \quad (3.5)$$

where μ_N is the largest eigenvalue of tensor A . If the above condition is violated, the transverse oscillation will be unstable which results in a 'zig-zag' crystal structure [33]. In this thesis, only the stable configuration is considered. The anharmonic coupling (3rd order) can be written in a compact form:

$$L_{ah} = -\frac{M\omega_3^2}{2l} \sum_{m,n,p=1}^N C_{mnp} \epsilon_{p3} (2\epsilon_{m3} \epsilon_{n3} - 3\epsilon_{m1} \epsilon_{n1} - 3\epsilon_{m2} \epsilon_{n2}), \quad (3.6)$$

where C_{mnp} is a rank-3 tensor and its explicit form is given in Appendix 8.1.

The classical motion due to the harmonic terms can be solved analytically by diagonalizing the positive definite tensors A, B [35]:

$$\begin{aligned} q'_{Am} &= Q_{Am} \cos(\nu_m t + \phi_{Am}), \\ q'_{Rm} &= Q_{Rm} \cos(\omega_m t + \phi_{Rm}), \end{aligned} \quad (3.7)$$

for the axial and radial harmonic motion. Here, q'_m is the m th component of displacement vector in normal coordinates, which corresponds to m th eigenmode and eigenfrequency of the axial/radial motion. Q_m, ϕ_m are constants determined by initial conditions and

$$\begin{aligned} \nu_m &= \omega_z \sqrt{\mu_m}, \\ \omega_m &= \omega_z \sqrt{\kappa_m}, \end{aligned} \quad (3.8)$$

are the axial and radial eigenfrequencies of the system, ν_m is the eigenvalue of A and κ_m is the eigenvalue of B with $m = 1, 2, \dots, N$. We label the COM mode for both axial and radial direction as $m = 1$, corresponding to the minimum ν_m and the maximum ω_m . The other modes

are labeled with their eigenvalues in increasing/decreasing orders for axial/radial directions, respectively. For instance, ν_2 for the second smallest axial eigenfrequency and ω_2 for the second largest radial eigenfrequency. The normal displacement vector \vec{q}' is related to the displacement \vec{q} in original coordinates defined in Figure 1 by:

$$\begin{aligned}\vec{q}_A &= \hat{U}_A \vec{q}'_A, \\ \vec{q}_R &= \hat{U}_R \vec{q}'_R.\end{aligned}\tag{3.9}$$

\hat{U} is a unitary transformation matrix that diagonalizes the corresponding elastic tensor with each column being an eigenvector of the tensor, $\hat{U}^T = \hat{U}^{-1}$. Also note that since $[A, B] = 0$, they share exactly the same set of eigenmodes but the corresponding eigenvalues will be different.

3.1.2 Quantum Hamiltonian

Consider the radial degree of freedom, in normal coordinates, the Hamiltonian is given by:

$$H = \sum_m \frac{M}{2} (\dot{q}'_m{}^2 + \omega_m^2 q'^2_m) = \sum_m \frac{p'^2_m}{2M} + \frac{M}{2} \omega_m^2 q'^2_m.\tag{3.10}$$

In the formalism of quantum ladder operators, this Hamiltonian can be rewritten as:

$$\hat{H} = \sum_m \omega_m \left(\hat{a}_m^\dagger \hat{a}_m + \frac{1}{2} \right),\tag{3.11}$$

where the ladder operators are defined as $\hat{a}_m = \sqrt{\frac{M\omega_m}{2}} \left(\hat{q}'_m + \frac{i\hat{p}'_m}{M\omega_m} \right)$ and $\hat{a}^\dagger = \sqrt{\frac{M\omega_m}{2}} \left(\hat{q}'_m - \frac{i\hat{p}'_m}{M\omega_m} \right)$. We denote $\hat{a}_m, \hat{b}_m, \hat{c}_m$ and the adjoint operators as ladder operators for the motion in the $\hat{z}, \hat{x}, \hat{y}$ directions, respectively. The harmonic part of motion Hamiltonian of the trapped-ion system is given by:

$$\hat{H}_h = \sum_{m=1}^N \nu_m \hat{a}_m^\dagger \hat{a}_m + \omega_m \left(\hat{b}_m^\dagger \hat{b}_m + \hat{c}_m^\dagger \hat{c}_m \right).\tag{3.12}$$

The anharmonic part of the system can be considered as a high order perturbation and expressed in the basis of the harmonic part, following the approximation made in Section 4.2 of [32]:

$$\hat{H}_{ah} = -3\varepsilon\omega_z \sum_{m,n,p=1}^N \frac{D_{mnp}}{(\mu_p \gamma_m \gamma_n)^{\frac{1}{4}}} \left[2\hat{a}_p \left(\hat{b}_m^\dagger \hat{b}_n + \hat{c}_m^\dagger \hat{c}_n \right) + \hat{a}_p \left(\hat{b}_m^\dagger \hat{b}_n^\dagger + \hat{c}_m^\dagger \hat{c}_n^\dagger \right) + h.c. \right],\tag{3.13}$$

where p is the index for axial modes, and m , and n are indices for radial modes. ω_z is the axial trap confining frequency and

$$\varepsilon = \frac{1}{4l_0} \sqrt{\frac{1}{2M\omega_z}}.$$

The tensor D is related to tensor C by

$$D_{pqr} = \sum_{l,m,n=1}^N C_{lmn} v_l^{(p)} v_m^{(q)} v_n^{(r)}.\tag{3.14}$$

Here $v_l^{(p)}$ represents the l -th element of the p -th eigenmode (same for transverse/axial vibration).

For convenience, we denote the sum of harmonic and anharmonic parts as the total motion Hamiltonian of the N-ion system:

$$\hat{H}_{motion} = \hat{H}_h + \hat{H}_{ah}. \quad (3.15)$$

For all models we are interested in, it will be sufficient to utilize one of the two radial vibrational degrees of freedom in terms of spin-phonon interactions (we choose the \vec{x} direction). Motion in the other direction (\vec{y}) can be neglected as they are not coupled to the spin part of the system. Therefore, in the following derivations, terms related to \hat{c} in \hat{H}_{motion} will be neglected.

3.2 Ion Interaction with Classical Light Field

In this section, we first construct the Hamiltonian for semi-classical dipole interactions of a single ion with a single laser drive or a set of two sideband drives in the radial direction. (In the actual experimental setup we will also apply drives in axial \vec{z} direction, which can be derived in a similar method.) Based on this, we derive the total Hamiltonian of the N ion system interacting with lasers. Then we further transform and simplify the results using some approximations.

3.2.1 Dipole Approximation

Assuming a laser field propagating in radial \vec{x} direction (we use \vec{x} instead of \hat{x} to avoid confusion with operators). Within semi-classical approximations the laser field is described by a classical EM wave:

$$\vec{E} = \vec{E}_0 \cos(\vec{k}\vec{r} - \omega_L t + \phi), \quad \vec{k} = k\vec{x}, \quad (3.16)$$

where ω_L is the laser frequency, k is the laser wavenumber. The index j is used to identify each ion interacting with the laser, and m is used for the phonon modes. We treat the ion as a two-level system [36]. The two states are described by the ionic Hamiltonian:

$$\hat{H}_{ion} = \sum_j \frac{\omega_0}{2} \hat{\sigma}_z^j, \quad \omega_0 = \omega_{hf}, \quad (3.17)$$

where ω_{hf} is the hyper-fine splitting frequency of Yb171 [33]. For the j th ion, the laser-ion interaction Hamiltonian is, under the dipole approximation, given by:

$$\hat{H}_I^j = -\hat{\vec{d}}_j \cdot \vec{E}, \quad (3.18)$$

where $\hat{\vec{d}}_j$ is the effective electric dipole moment for ion j , The Rabi frequency is defined by [31]:

$$\Omega_j \equiv \langle g | \hat{\vec{d}}_j \cdot \vec{E}_0 | e \rangle. \quad (3.19)$$

Here, $|g\rangle, |e\rangle$ are the ground and excited states of the ion, respectively. The explicit expression for the interaction Hamiltonian is:

$$\hat{H}_I^j = \frac{\Omega_j}{2} (\hat{\sigma}_j^- + \hat{\sigma}_j^+) \left(e^{i(\vec{k} \cdot \vec{r}_j - \omega_L t + \phi)} + e^{-i(\vec{k} \cdot \vec{r}_j - \omega_L t + \phi)} \right) = \frac{\Omega_j}{2} \hat{H}_{sI}^j \hat{H}_{pI}^j. \quad (3.20)$$

where we defined the spin and phonon interaction Hamiltonian as:

$$\hat{H}_{sI}^j \equiv (\hat{\sigma}_j^- + \hat{\sigma}_j^+), \quad \hat{H}_{pI}^j \equiv \frac{\Omega_j}{2} \left(e^{i(\vec{k} \cdot \vec{r}_j - \omega_L t + \phi)} + e^{-i(\vec{k} \cdot \vec{r}_j - \omega_L t + \phi)} \right).$$

We rewrite $\widehat{\vec{r}}_j \equiv \vec{r}_j + \widehat{\vec{e}}_j$ in terms of displacement from equilibrium. The scalar $\vec{k} \cdot \vec{r}_j$ can be absorbed into the phase as it remains constant. We denote:

$$\vec{k} \cdot \widehat{\vec{r}}_j \rightarrow \vec{k} \cdot \widehat{\vec{e}}_j = k\hat{x}_j, \quad x_j = \sum_m T_{jm} X_m, \quad (3.21)$$

where x_j is expanded in terms of normal coordinates X_m , $T_R = [v_1, \dots, v_N]$ is the radial similarity transformation matrix, as discussed in Eq. (3.9) and T_{jm} is the j, m th index of T_R . Using the formalism of ladder operators, $\hat{X}_m = X_{0m}(\hat{b}_m^\dagger + \hat{b}_m)$, with $X_{0m} \equiv \sqrt{1/2M\omega_m}$ being the characteristic length scale of mode m . We define the tensor

$$\zeta_{im} \equiv kT_{jm}X_{0m}. \quad (3.22)$$

Recalling that $\vec{k} = (k, 0, 0)$, we can rewrite the displacement operator in the form:

$$\vec{k} \cdot \widehat{\vec{r}}_j = \sum_{m=1}^N \zeta_{jm} (\hat{b}_m^\dagger + \hat{b}_m). \quad (3.23)$$

The total Hamiltonian of the system can be then obtained by combining Eqs. (3.15), (3.17), and (3.20):

$$\hat{H} = \hat{H}_{ion} + \hat{H}_{motion} + \hat{H}_I. \quad (3.24)$$

3.2.2 Ordinary Interaction Frame

We simplify Eq. (3.24) by rotating into an “ordinary” interaction frame in which \hat{H}_h, \hat{H}_{ion} are cancelled out. We therefore define unitary operator:

$$\hat{U}(t) = \exp(-i\hat{H}_0 t), \quad \hat{H}_0 = \hat{H}_{ion} + \hat{H}_h, \quad (3.25)$$

The Hamiltonian in the new interaction frame is given by the transformation [31]:

$$\hat{H}' = i \left(\frac{\partial}{\partial t} \hat{U}^\dagger \right) \hat{U} + \hat{U}^\dagger \hat{H} \hat{U}, \quad (3.26)$$

because $[\hat{H}_0, \hat{U}(t)] = 0, i \left(\frac{\partial}{\partial t} \hat{U}^\dagger \right) \hat{U} = 0$,

$$\begin{aligned} \hat{H}' &= \hat{U}^\dagger \left(\sum_{j=1}^N \hat{H}_I^j + \hat{H}_{ah} \right) \hat{U} \\ &= \hat{H}'_I + \hat{H}'_{ah}. \end{aligned} \quad (3.27)$$

In the following derivation we neglect the ion index j for simplicity. This index will be recovered again at the end of this subsection. We first derive the form of ion-laser interaction term and then derive the form of anharmonic term in this frame. For detailed derivations of Eqs. (3.28), (3.29), see Appendix B. The transformation of spin part of \hat{H}_I is given by:

$$\begin{aligned} \hat{U}^\dagger \hat{H}_{sI} \hat{U} &= e^{\frac{i\omega_0 t}{2} \hat{\sigma}_z} \hat{\sigma}_x e^{-\frac{i\omega_0 t}{2} \hat{\sigma}_z} \\ &= e^{i\omega_0 t} \hat{\sigma}^+ + e^{-i\omega_0 t} \hat{\sigma}^-. \end{aligned} \quad (3.28)$$

The transformation of the phonon part can be derived in Lamb-Dicke Regime ($kX_{0m} \ll 1$):

$$\begin{aligned}\hat{U}^\dagger \hat{H}_{mI} \hat{U} &= \frac{\Omega}{2} \hat{I} \left[e^{-i(\omega_L t - \phi)} + e^{i(\omega_L t - \phi)} \right] \\ &+ \frac{\Omega}{2} \sum_m i\zeta_m \left(\hat{b}_m^\dagger e^{i\omega_m t} + \hat{b}_m e^{-i\omega_m t} \right) \hat{\sigma}^+ e^{-i(\delta t - \phi)} \\ &+ \frac{\Omega}{2} \sum_m -i\zeta_m \left(\hat{b}_m^\dagger e^{i\omega_m t} + \hat{b}_m e^{-i\omega_m t} \right) \hat{\sigma}^- e^{i(\delta t - \phi)}.\end{aligned}\quad (3.29)$$

Let us combine the above transformations for spin and phonon parts and define $\delta = \omega_L - \omega_0$, with Rotating Wave Approximation (RWA)

$$\omega_0 + \omega_L \gg |\omega_0 - \omega_L| = |\delta| \quad (3.30)$$

$$\begin{aligned}\hat{U}^\dagger (\hat{H}_{sI} \hat{H}_{mI}) \hat{U} &= \frac{\Omega}{2} \hat{I} \left[\hat{\sigma}^+ e^{-i(\delta t - \phi)} + \hat{\sigma}^- e^{i(\delta t - \phi)} \right] \\ &+ \frac{\Omega}{2} \sum_m i\zeta_m \left(\hat{b}_m^\dagger e^{i\omega_m t} + \hat{b}_m e^{-i\omega_m t} \right) \hat{\sigma}^+ e^{-i(\delta t - \phi)} \\ &+ \frac{\Omega}{2} \sum_m -i\zeta_m \left(\hat{b}_m^\dagger e^{i\omega_m t} + \hat{b}_m e^{-i\omega_m t} \right) \hat{\sigma}^- e^{i(\delta t - \phi)},\end{aligned}\quad (3.31)$$

where ω_m is the angular radial eigenfrequency defined in (3.8).

For a single drive at frequency $\omega_L = \omega_0$, $\delta = 0$, the first term in (3.31) is at resonance, the second and third terms rotate at $\omega_m/2\pi \sim \text{MHz}$. This type of drive can be used to generate pure spin operators in form:

$$\frac{\Omega}{2} \left[\hat{\sigma}^+ e^{i\phi} + \hat{\sigma}^- e^{-i\phi} \right]. \quad (3.32)$$

If a set of sideband laser drives at frequencies μ such that

$$\omega_b = \omega_0 + \mu, \quad \omega_r = \omega_0 - \mu, \quad (3.33)$$

are applied, the second and third term in Eq.(3.31) can be resonantly addressed. Let us substitute ω_L with ω_b, ω_r , the second and third term in (3.31) become:

$$\begin{aligned}\hat{H}_b &= \frac{\Omega}{2} \left[\sum_m i\zeta_m \left(\hat{b}_m^\dagger e^{i\omega_m t} + \hat{b}_m e^{-i\omega_m t} \right) \hat{\sigma}^+ e^{-i(\mu t - \phi_b)} - \sum_m i\zeta_m \left(\hat{b}_m^\dagger e^{i\omega_m t} + \hat{b}_m e^{-i\omega_m t} \right) \hat{\sigma}^- e^{i(\mu t - \phi_b)} \right] \\ \hat{H}_r &= \frac{\Omega}{2} \left[\sum_m i\zeta_m \left(\hat{b}_m^\dagger e^{i\omega_m t} + \hat{b}_m e^{-i\omega_m t} \right) \hat{\sigma}^+ e^{i(\mu t + \phi_r)} - \sum_m i\zeta_m \left(\hat{b}_m^\dagger e^{i\omega_m t} + \hat{b}_m e^{-i\omega_m t} \right) \hat{\sigma}^- e^{-i(\mu t + \phi_r)} \right].\end{aligned}\quad (3.34)$$

Summing over these two terms:

$$\begin{aligned}\hat{H}'_I &= \hat{H}_r + \hat{H}_b \\ &= \Omega \sum_m \zeta_m \hat{\sigma}^{\phi_s} \cos(\mu t - \phi_m) (\hat{b}_m e^{-i\omega_m t} + \hat{b}_m^\dagger e^{i\omega_m t}),\end{aligned}\quad (3.35)$$

where

$$\hat{\sigma}^{\phi_s} = \hat{\sigma}^+ e^{i\phi_s} - \hat{\sigma}^- e^{-i\phi_s}.$$

The phase factors are defined as:

$$\phi_m = \frac{1}{2}(\phi_b - \phi_r), \quad \phi_s = \frac{1}{2}(\phi_b + \phi_r) + \frac{\pi}{2}.$$

The first term of (3.31) rotates at $|\delta| = \mu \sim \omega_m \sim \text{MHz}$ for experimental setup and it only couples to spin degrees of freedom. When pure spin operators are applied, this term can be considered as fast varying and its effect can be neglected.

Recovering the index of ions coupled to the laser j , we have:

$$\hat{H}'_I = \sum_j \Omega_j \hat{\sigma}_j^{\phi_s} \sum_{m=1}^N \zeta_{jm} \cos(\mu t - \phi_m) (\hat{b}_m e^{-i\omega_m t} + \hat{b}_m^\dagger e^{i\omega_m t}) \quad (3.36)$$

For the anharmonic term, using Eq. (3.13) it can be shown that (see Appendix A):

$$\hat{H}'_{ah} = -3\varepsilon\omega_z \sum_{m,n,p=1}^N \left[\frac{D_{mnp}}{(\gamma_m \gamma_n \mu_p)^{\frac{1}{4}}} \left(2\hat{a}_p \hat{b}_m^\dagger \hat{b}_n e^{-i\Delta_{mnp}^- t} + \hat{a}_p \hat{b}_m^\dagger \hat{b}_n^\dagger e^{i\Delta_{mnp}^+ t} \right) + \text{h.c.} \right]. \quad (3.37)$$

The rotating frequencies are defined as:

$$\Delta_{mnp}^\pm = \omega_m \pm \omega_n - \nu_p. \quad (3.38)$$

As a short summary, the total Hamiltonian in ordinary frame will be composed of Eq. (3.32) (pure spin), Eq. (3.36) (spin-phonon coupling), Eq. (3.37) (anharmonicity).

4 Mapping to Target Models

In this section we will show how the total Hamiltonian of trapped-ion system can map to the target models in Section 2. We start with a general discussion of how to create the desired spin operators and our capability of creating anharmonic coupling between different modes. Then we introduce the resonant interaction frame and show how the time-independent Hamiltonian in each model can be realized.

For all models, we use a system of 3 ions as a prototype simulator. Compared to the configuration of Ref. [30], it has richer set of eigenmodes (3 modes in each vibrational degree of freedom) such the physics of different target models can be captured. This configuration could also be easily realized experimentally in terms of stable confinement. Under appropriate approximations, this system is small enough such that it is still within the capability of a classical computer, which makes the numerical simulations available.

4.1 Spin-only Operators

To map to the target models, $\hat{\sigma}_x$ and $\hat{\sigma}_z$ operators need to be realized simultaneously. By applying drives at $\omega_L = \omega_{hf}$ it is possible to create a $\frac{\Omega'}{2}\hat{\sigma}_x$ term by setting the spin phase $\phi_s = \pi/2$ and $-\frac{\Omega'}{2}\hat{\sigma}_y$ by setting $\phi_s = 0$. By applying a global rotation

$$\hat{R}_x(\pi/2) = \exp(-i\hat{\sigma}_x\pi/2), \quad (4.1)$$

we can rotate into σ_y eigenbasis:

$$\begin{aligned}\frac{\Omega'}{2}\hat{\sigma}_x &\rightarrow \frac{\Omega'}{2}\hat{\sigma}_x, \\ -\frac{\Omega'}{2}\hat{\sigma}_y &\rightarrow \frac{\Omega'}{2}\hat{\sigma}_z.\end{aligned}\tag{4.2}$$

For the spin-phonon coupling term in Eq. (3.36), we set $\phi_s = 0$, $\phi_m = 0$ by choosing the sideband phases to be $\phi_r = \phi_b = -\pi/2$. The same rotation will transform $\hat{\sigma}_y$ operator to $\hat{\sigma}_z$. The electronic coupling coefficients mentioned for these terms are determined by the Rabi frequency Ω , which can be controlled by tuning the power of laser drives applied.

4.2 Donor-Acceptor Pair System

Two equivalent Hamiltonians for Donor-Acceptor pair system have been discussed in Section 2. In order to map Eq. (3.36) to the phonon and spin-phonon coupling part in Eqs. (2.1) and (2.5), we follow the procedure in [37] and rotate into a “resonant” interaction frame in which the Hamiltonian of the ion chain becomes time-independent. Consider a set of 2 sideband radial drives with frequencies defined in Eq. (3.33) and assume all anharmonic terms are detuned off-resonance so that the anharmonic coupling can be neglected. By adding and subtracting a term $\hat{H}_\delta = \sum_m \delta_m \hat{b}_m^\dagger \hat{b}_m$, the total Hamiltonian becomes:

$$\hat{H} = (\hat{H}_{ion} + \hat{H}_h + \hat{H}_\delta) + (\hat{H}_I - \hat{H}_\delta).\tag{4.3}$$

We redefine the unitary transformation in Eq. (3.25) with

$$\begin{aligned}\hat{U}_{res}(t) &= \exp\left(-i\hat{H}_0^{res}t\right), \\ \hat{H}_0^{res} &= \hat{H}_{ion} + \hat{H}_h + \hat{H}_\delta = \hat{H}_{ion} + \mu \sum_m \hat{b}_m^\dagger \hat{b}_m.\end{aligned}\tag{4.4}$$

The Hamiltonian of the ion system in this new frame becomes

$$\begin{aligned}\hat{H}_I^{res} &= \hat{U}_{res}^\dagger \left(\hat{H}_I - \hat{H}_\delta \right) \hat{U}_{res} \\ &= \sum_j \frac{\Omega_j}{2} \hat{\sigma}_j^{\phi_s} \sum_m \zeta_m \left[\hat{b}_m \left(e^{-i\phi_m} + e^{-i(2\mu t - \phi_m)} \right) + \hat{b}_m^\dagger \left(e^{i\phi_m} + e^{i(2\mu t - \phi_m)} \right) \right] - \sum_{m=1}^N \delta_m \hat{b}_m^\dagger \hat{b}_m,\end{aligned}\tag{4.5}$$

(see Appendix 8.2 for derivation).

Within the RWA, we can neglect off-resonant terms rotating at 2μ . The condition for this RWA needs to be deduced from Eq. (3.36) in resonant frame. The actual approximation made is neglecting the term rotating at $\mu + \omega_m$ by assuming:

$$|\mu - \omega_m| = \delta_m \ll \mu + \omega_m.\tag{4.6}$$

Therefore, a small detuning δ_m is favorable for generating a time-independent Hamiltonian. With this approximation, we do a global rotation and adjust the phase following Eq. (4.1), obtaining:

$$\hat{H}_I^{res} = \sum_j \frac{\Omega_j}{2} \hat{\sigma}_j^z \sum_{m=1}^N \zeta_{jm} \left(\hat{b}_m + \hat{b}_m^\dagger \right) - \sum_{m=1}^N \delta_m \hat{b}_m^\dagger \hat{b}_m.\tag{4.7}$$

The detuning can be set negative $\delta_m < 0$ by adjusting the applied laser frequency, so that \hat{H}_I^{res} has exactly the same form as the phonon and spin-phonon term in Eqs. (2.1) and (2.5).

Figure 2 shows setup of simulator for the two site system in (2.1). In our 3-ion prototype simulator ion 1 and ion 2 are assigned to be the two molecular sites. Two resonant single radial drives as described in Eq. (4.1) can be applied on ion 1, ion 2, respectively, creating $E_1 \hat{\sigma}_z^1 + E_2 \hat{\sigma}_z^2$ term with $E_1 > E_2$. Details on generating spin exchange term $J_{12}(\hat{\sigma}_1^+ \hat{\sigma}_2^- + h.c.)$ is discussed in section 2.3.3 of Ref. [38]. As described above, a set of sideband radial drives will generate phonon and spin-phonon coupling terms. We set the effective frequency $\mu \lesssim \delta_r$ such that all $\delta_m < 0$. The total Hamiltonian for this two-site simulator is then given by:

$$\hat{H} = \sum_{j=1}^2 E_j \hat{\sigma}_z^j + J_{12} (\hat{\sigma}_1^+ \hat{\sigma}_2^- + h.c.) + \sum_{j=1}^2 \frac{\Omega_j}{2} \hat{\sigma}_j^z \sum_{m=1}^N \zeta_{jm} (\hat{b}_m + \hat{b}_m^\dagger) - \sum_{m=1}^N \delta_m \hat{b}_m^\dagger \hat{b}_m. \quad (4.8)$$

The remaining ion 3 will serve as a coolant to induce the dissipation in Eq. (2.3) by applying Raman sideband cooling. By applying continuous red sideband on the coolant ion at eigenfrequency ω_m can effectively generate annihilation \hat{b}_m operator on mode m with cooling rate controlled by the corresponding Rabi frequency and tensor element ζ_{jm} (see Section 2.3.6 of [33] for details). To ensure this sideband is only coupled to the coolant ion, we can implement individual addressing or sympathetic cooling (using different isotopes for coolant and site ions, see [39]). Under this cooling scheme, the phonon modes of the ion-system can be considered as an effective external reservoir. The Lindbladian in Eq. (2.3) then takes form [30]:

$$\hat{L}(\hat{\rho}) = \sum_m \gamma_m (1 + \bar{n}_m) \left(\hat{b}_m \hat{\rho} \hat{b}_m^\dagger - \frac{1}{2} [\hat{b}_m^\dagger \hat{b}_m, \hat{\rho}] \right) + \gamma_m \bar{n}_m \left(\hat{b}_m^\dagger \hat{\rho} \hat{b}_m - \frac{1}{2} [\hat{b}_m \hat{b}_m^\dagger, \hat{\rho}] \right), \quad (4.9)$$

where γ is an effective cooling rate controlled by laser power and \bar{n}_m is the average phonon number of vibrational mode m at given thermal temperature T .

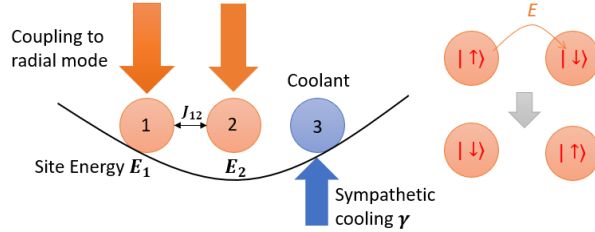


Figure 2: Experimental scheme for simulating two-site donor-acceptor pair system. Ion 1,2 are $^{171}\text{Yb}^+$ assigned as molecular sites while ion 3 is $^{172}\text{Yb}^+$ used as a coolant. The initial and final spin states in a typical EET are shown on the right.

Crucially the effective cooling rate has a dependence on ζ , therefore choosing a different ion as coolant will result in different cooling rates. For instance, it is not possible to effectively generate dissipation on the tilt mode if ion 2 is used as the coolant ($\zeta_{22} = 0$). Assuming the coolant index is j' , to make the simulation more realistic, we explicitly add this dependence by further modifying the Lindbladian to:

$$\hat{L}(\hat{\rho}) = \sum_m |T_{j'm}| \gamma_m (1 + \bar{n}_m) \left(\hat{b}_m \hat{\rho} \hat{b}_m^\dagger - \frac{1}{2} [\hat{b}_m^\dagger \hat{b}_m, \hat{\rho}] \right) + |T_{j'm}| \gamma_m \bar{n}_m \left(\hat{b}_m^\dagger \hat{\rho} \hat{b}_m - \frac{1}{2} [\hat{b}_m \hat{b}_m^\dagger, \hat{\rho}] \right), \quad (4.10)$$

$T_{j'm}$ is the element of unitary transformation matrix as defined in (3.22). In a similar way we can map the simulator to one-site equivalent system following the scheme in Figure 3. We therefore can set just ion 1 as a molecular site while the other two ions provides the vibrational modes for the system. Ion 3 again serves as the coolant while ion 2 has the only function of enriching the vibrational mode structure. The terms $\frac{\Delta E}{2}\hat{\sigma}_z + V\hat{\sigma}_x$ in Eq. (2.5) can be constructed with 2 resonant drives applied on ion 1 with appropriate phases while phonon and spin-phonon coupling terms are generated as explained above. The total Hamiltonian for a one-site simulator is given by:

$$\frac{\Delta E}{2}\hat{\sigma}_z + V\hat{\sigma}_x + \sum_j \frac{\Omega_j}{2}\hat{\sigma}_j^z \sum_{m=1}^N \zeta_{jm} (\hat{b}_m + \hat{b}_m^\dagger) - \sum_{m=1}^N \delta_m \hat{b}_m^\dagger \hat{b}_m. \quad (4.11)$$

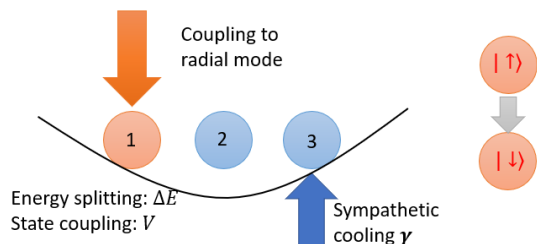


Figure 3: Experimental scheme for simulating one-site donor-acceptor pair system. Ion 1 is $^{171}\text{Yb}^+$ assigned as molecular site while ion 2, 3 are $^{172}\text{Yb}^+$ and ion 3 is assigned as a coolant. The initial and final spin states in a typical EET are shown on the right.

The two-site system is currently not realizable for our lab since we are not capable of applying individual laser addressing to the ions at the moment. The one-site system is experimentally favorable. We can use $^{171}\text{Yb}^+$ for ion 1 $^{172}\text{Yb}^+$ for ion 2, 3 so that the global resonant and sideband drives would only couple to ion 1. For purpose of this project, we will do numerical simulations to explore the properties of the two-site system coupled to multiple phonon modes and show its equivalence to the well-studied one-site systems. These simulations will also serve as a benchmark for our numerical methods.

4.3 Anharmonic Phonon Coupling

Eqs. (3.37) and (3.38) show that we are able to set anharmonic couplings for one specific set of modes m, n, p on resonance by tuning the trap frequencies. The resonance condition is given by setting one of $\Delta_{mnp}^\pm = 0$. Also note that only a few of the coupling coefficients are non-zero due to the symmetry of tensor D (see Fig. 4). A table of numerical values of D_{mnp} can be found in [32] for different ion numbers.

For the prototype simulator, we follow the same setup as in Ref. [40]. We choose $m = n = 3$, $p = 2$ and create a Fermi-resonant coupling between radial rocking mode and axial tilt mode. This will give a simple form of resonance condition and a time-independent anharmonic term in the resonant frame to be introduced:

$$\Delta_{332}^+ = 2\omega_3 - \nu_2 = 0. \quad (4.12)$$

The trap frequency under this resonance condition can be solved analytically for 3-ion system:

$$f_z = \sqrt{\frac{20}{63}} f_x. \quad (4.13)$$

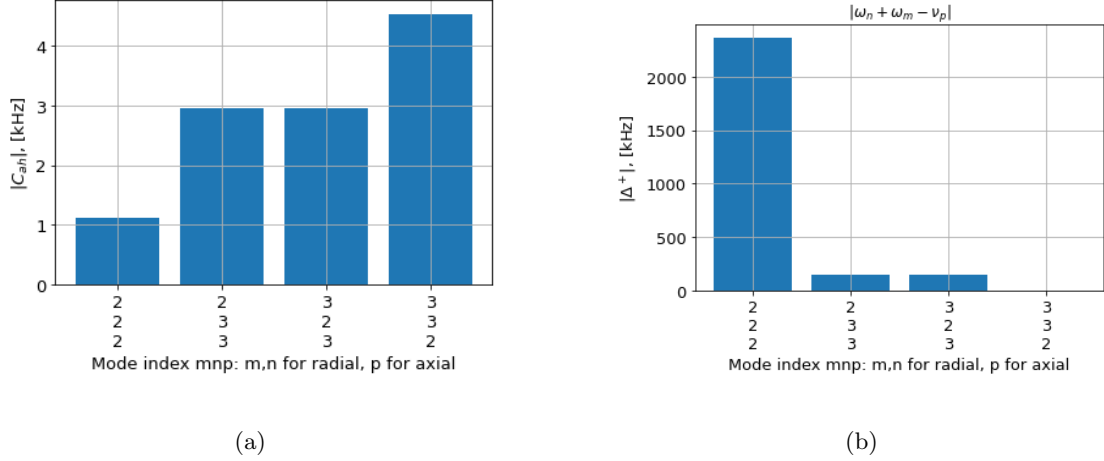


Figure 4: Plot of non-zero anharmonic coupling coefficients and corresponding oscillating frequencies, with trap confine frequencies $f_x = 3.50$ MHz, $f_z = 1.97$ MHz such that $[3, 3, 2]$ is resonant. The non-zero anharmonic terms are $[m, n, p] = [2, 2, 2], [2, 3, 3], [3, 2, 3], [3, 3, 2]$ for a system of 3 ions. (b) shows the smallest off-resonance Δ_{mnp}^+ is on the order of 0.1 MHz

The term $\Delta^- = -\nu_p \sim$ MHz while the other sets of modes has $\Delta_{mnp}^+ \gtrsim 0.1$ MHz (Fig. 4) with RWA we can neglect the term oscillating at all other frequencies in (3.37), the anharmonic term becomes:

$$\begin{aligned} \hat{H}'_{ah} &= C_{ah}(a_t^\dagger b_r b_r + a_t b_r^\dagger b_r^\dagger), \\ C_{ah} &= -3\varepsilon\omega_z \frac{D_{332}}{(\gamma_3\gamma_3\mu_2)^{\frac{1}{4}}}. \end{aligned} \quad (4.14)$$

Here we use label r, t , for operators on radial rocking mode and axial tilt mode, respectively.

The magnitude of coupling coefficient C_{ah} only depends on the trap frequency. The direct modulation of C_{ah} is restricted because the appropriate operating regime of the trap for stable confinement in our lab is 2 to 4 MHz for f_x . However, we can effectively tune the coupling strength by shifting away from the resonance with an increasing anharmonic detuning defined as:

$$\delta_{ah} = 2\omega_3 - \nu_2. \quad (4.15)$$

We also investigate possible resonance anharmonic coupling in configurations of more than 3 ions. In this case not all non-zero D_{mnp} are realizable in a stable configuration and there is no analytical solution for the eigenfrequencies. For a given radial confining frequency f_x and mode index $[m, n, p]$, we compute resonant f_z by numerically solving:

$$\omega_m + \omega_n - \nu_p = 0, \quad (4.16)$$

under the constraint of stability condition from Eq.(3.5).

4.4 Anharmonic Spin-phonon System with Two Drives

The first type of trapped-ion setup for the anharmonic system discussed in section 2.2 involves 2 sideband drives coupling to axial and radial directions, respectively. The experimental scheme

is shown in Fig.5. From numerical simulations we found this setup that is most likely to induce delocalization. Related details will be discussed in section 5. The spin part in Eqs. (2.7), (2.8) can be created in the same way as in section 4.3. For the remaining part of the target Hamiltonian, consider two distinctive sets of sideband drives:

$$\omega_{Lbl} = \omega_0 + \mu_l, \omega_{Lrl} = \omega_0 - \mu_l. \quad (4.17)$$

with electric field index labeled by $l = 1, 2$ for axial and radial directions.

Using Eqs. (3.25), (3.26), the laser-ion interaction Hamiltonian in ordinary interaction frame is given by:

$$\begin{aligned} \hat{H}'_I &= \hat{H}'_{Ix} + \hat{H}'_{Iz} \\ &= \sum_j \Omega_{1j} \sum_{m=1}^N \eta_{jm} \hat{\sigma}_j^{\phi_s} \cos(\mu_1 t - \phi_{1m}) (\hat{a}_m e^{-i\nu_m t} + \hat{a}_m^\dagger e^{i\nu_m t}) \\ &\quad + \sum_j \Omega_{2j} \sum_{m=1}^N \zeta_{jm} \hat{\sigma}_j^{\phi_s} \cos(\mu_2 t - \phi_{2m}) (\hat{b}_m e^{-i\omega_m t} + \hat{b}_m^\dagger e^{i\omega_m t}), \end{aligned} \quad (4.18)$$

ζ follows the same definition as in section 3.2 and $\eta_{jm} = k_1 T_{A,jm} Z_{0m}$, T_A is the similar transformation matrix where each column vector is the transverse eigenmode of the elastic tensor A for axial motion, $Z_{0m} = \sqrt{1/2M\nu_m}$ is the characteristic length scale of mode m in axial direction. \hat{a}_m is the phonon ladder operator for axial mode m .

The anharmonic term transform into Eq. (3.37) with resonant coupling condition given by Eq. (3.38). In the same way as previous section we can rotate into resonant interaction frame by defining:

$$\begin{aligned} \hat{H}_\delta &= \sum_m (\delta_{Am} \hat{a}_m^\dagger \hat{a}_m + \delta_{Rm} \hat{b}_m^\dagger \hat{b}_m) \\ \hat{H}_{tot} &= (\hat{H}_{ion} + \hat{H}_h + \hat{H}_\delta) + (\hat{H}_I + \hat{H}_{ah} - \hat{H}_\delta) \\ \hat{U}_{res}(t) &= \exp(-i\hat{H}_0^{res} t), \end{aligned} \quad (4.19)$$

$\delta_{Am} = \mu_1 - \nu_m$, $\delta_{Rm} = \mu_2 - \omega_m$ are the detunings from axial and radial eigenfrequencies. The anharmonic term will transform into:

$$\hat{H}_a^{res} = -3\varepsilon\omega_A \sum_{m,n,p=1}^N \left[\frac{D_{mnp}}{(\gamma_m \gamma_n \mu_p)^{1/4}} (2\hat{a}_p \hat{b}_m^\dagger \hat{b}_n e^{-i\mu_1 t} + \hat{a}_p \hat{b}_m^\dagger \hat{b}_n^\dagger e^{i(2\mu_2 - \mu_1)t}) + h.c. \right]. \quad (4.20)$$

The resonance condition is given by:

$$2\mu_2 - \mu_1 = 0, \quad 2(\omega_x + \delta_{Rcom}) = (\omega_z + \delta_{Acom}). \quad (4.21)$$

After choosing the appropriate phase and the global rotation, the total Hamiltonian of the

trapped-ion system is given by:

$$\begin{aligned}
\hat{H}_{tot}^{res} = & \sum_j \frac{\Delta E_j}{2} \hat{\sigma}_j^z + \sum_j V_j \hat{\sigma}_j^x \\
& + \sum_j \frac{\Omega_{1j}}{2} \hat{\sigma}_j^z \sum_{m=1}^N \eta_{jm} (\hat{a}_m + \hat{a}_m^\dagger) - \sum_{m=1}^N \delta_{Am} \hat{a}_m^\dagger \hat{a}_m \\
& + \sum_{j=1}^N \frac{\Omega_{2j}}{2} \hat{\sigma}_j^z \sum_{m=1}^N \zeta_{jm} (\hat{b}_m + \hat{b}_m^\dagger) - \sum_{m=1}^N \delta_{Rm} \hat{b}_m^\dagger \hat{b}_m \\
& - 3\varepsilon\omega_A \sum_{m,n,p=1}^N \left[\frac{D_{mnp}}{(\gamma_m \gamma_n \mu_p)^{1/4}} \hat{a}_p \hat{b}_m^\dagger \hat{b}_n^\dagger + h.c. \right]
\end{aligned} \tag{4.22}$$

here we assume resonant condition $2\mu_1 = \mu_2$ is satisfied and neglect off-resonant anharmonic terms. Using individual addressing or using different isotopes this Hamiltonian will take a similar format as Eq. (2.7) and with global laser drives we can map to Eq. (2.8).

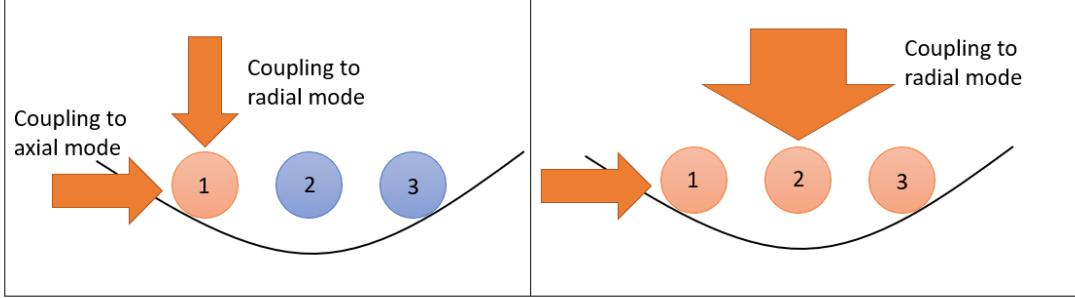


Figure 5: Left: Experimental scheme for simulating anharmonic spin-phonon system with one-site and 2 drives. Ion 1 is $^{171}\text{Yb}^+$ assigned as molecular site while ion 2,3 are $^{172}\text{Yb}^+$ used to provide vibrational modes. Right: Experimental scheme for simulating anharmonic spin-phonon system with three sites and two drives. All three ions are $^{171}\text{Yb}^+$ assigned as molecular site and used to provide vibrational modes.

4.5 Anharmonic Spin-phonon system with One Drive

The second type of trapped-ion setup for the anharmonic system discussed in section 2.2 involves a single set of sideband drives coupling to radial direction. The experimental scheme is shown in Figure 6. In the ordinary frame, the spin-phonon, and anharmonic coupling term will take the same form as Eq. (3.36) and (3.37). To rotate into resonant frame we use the same procedure as in Eq. (4.19). In this case since there is no spin-phonon coupling in axial direction, so δ_{Am} is not defined. Instead, an arbitrary real number Δ_m can be chosen for each axial mode and we can define a pseudo effective frequency $\Lambda_m = \Delta_m + \nu_m$ accordingly:

$$\hat{H}_\delta = \sum_m -(\Delta_m \hat{a}_m^\dagger \hat{a}_m + \delta_m \hat{b}_m^\dagger \hat{b}_m). \tag{4.23}$$

After choosing the appropriate phase and global rotation, the total Hamiltonian of the trapped-ion system including pure spin operators becomes:

$$\begin{aligned} \hat{H}_{tot}^{res} = & \sum_j \frac{\Delta E_j}{2} \hat{\sigma}_j^z + \sum_j V_j \hat{\sigma}_j^x - \sum_{m=1}^N (\Delta_m \hat{a}_m^\dagger \hat{a}_m + \delta_m \hat{b}_m^\dagger \hat{b}_m) \\ & + \sum_j \frac{\Omega_j}{2} \hat{\sigma}_j^z \sum_{m=1}^N \zeta_{jm} (\hat{b}_m + \hat{b}_m^\dagger) - 3\varepsilon\omega_A \sum_{m,n=1}^N \left[\frac{D_{mnp'}}{(\gamma_m \gamma_n \mu_{p'})^{1/4}} \hat{a}_{p'} \hat{b}_m^\dagger \hat{b}_n^\dagger + h.c. \right], \end{aligned} \quad (4.24)$$

here we assume resonance condition $2\mu - \Lambda_p = 0$ is satisfied for a certain $p = p'$ and neglect the fast rotating off-resonance terms. Eq. (4.24) again takes a similar format as Eqs. (2.7), (2.8) when the appropriate drives are applied to the ions.

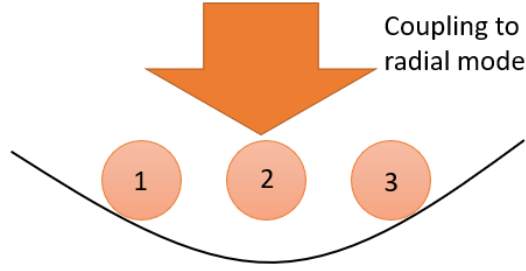


Figure 6: Experimental scheme for simulating anharmonic spin-phonon system with three sites and one drive. All three ions are $^{171}\text{Yb}^+$ assigned as molecular site and used to provide vibrational modes.

4.6 Summary

The correspondence between parameters of target models and their counter parts in trapped-ion system are summarized in Table 1. By individual addressing or using different isotopes, we control which ions are coupled to the laser (j index). We can also drive a specific mode (m index) in phonon-related interactions by parking the effective frequency μ near the eigenfrequency of a certain phonon mode. This becomes obvious in the ordinary frame. Spin-phonon interaction in Eq. (3.36) is dominated by the term oscillating at minimum detuning $\delta_{m,min}$. Interactions with other modes can be neglected when $\delta_{m,min}$ is sufficiently small.

For the resonant frame, all modes seems to be at resonance in Eq. (4.7) but they are suppressed by the additional harmonic term $-\sum_{m=1}^N \delta_m \hat{b}_m^\dagger \hat{b}_m$ so the time evolution will be the same as the ordinary frame. The same reasoning could explain the different resonance conditions for anharmonic coupling in the two frames. Consider the system in Eq. (4.22) and assume we setup the trap appropriately such that there is a resonance coupling between axial tilt and radial rocking mode (see discussion in section 4.2). In resonant frame we can enforce resonance for all combinations of mode index $[m, n, p]$ by tuning effective frequencies to $2\mu = \nu$. However, the effective coupling is still between modes $m = n = 3, p = 2$ under the suppression of $-\sum_{m=1}^N \delta_{Am} \hat{a}_m^\dagger \hat{a}_m - \sum_{m=1}^N \delta_{Rm} \hat{b}_m^\dagger \hat{b}_m$.

Target Model	Trapped-ion System
Site Energy/Energy Difference ΔE	Resonant Drive Rabi Frequency Ω_{res}
Electronic-vibrational coupling g, λ	sideband Drive Rabi Frequency Ω_{side}
Harmonic Vibrational Energy ω	sideband Detuning $-\delta$
Anharmonic Vibrational Energy Θ	Resonant Coupling Coefficient $-3\varepsilon\omega_A \frac{D_{mnp}}{(\gamma_m\gamma_n\mu_p)^{1/4}}$
Incoherent phonon dissipation rate Γ	Effective sideband cooling rate $ T_{j'm} \gamma$

Table 1: Correspondence between parameters of target models and their counter parts in trapped-ion system

5 Methods

In this section we discuss the numerical methods used in this work. First we illustrate some general approximations to be implemented in numerical simulations and review the equations to be solved for computing time evolution. We then discuss other helpful techniques including eigenenergy diagrams and various signatures of quantum delocalization.

A python module was built based on “Qutip” [41], “Numpy”, “Scipy”. It can be used to calculate trapped ion parameters and construct numerical forms of interaction Hamiltonian in a systematic way.

5.1 Approximations of Hamiltonian

We represent the spin part of the interaction Hamiltonian in a tensor product basis of multiple spin 1/2 space and the phonon part in a fock basis $\{|n\rangle\}$. Mathematically a phonon space has infinite dimensions. However, a finite cutoff p_c can be chosen when the phonon population is sufficiently small such that the phonon occupation at large n is negligible. In practice we first make a reasonable guess of p_c based on phonon population of initial state and solve for time evolution. Then we compute an error parameter defined as the maximum phonon population at highest allowed phonon state:

$$P_{err} = \langle |p_c\rangle \langle p_c| \rangle_{max}. \quad (5.1)$$

We readjust p_c until $P_{err} \lesssim 10^{-10}$ so that this finite cutoff would correctly capture the dynamics of the system. The Hamiltonian for a system of N spin 1/2 space and N' phonon space with individual cutoff set to $p_{c,m}$ has size:

$$(2^N \cdot \prod_{m=1}^{N'} p_{c,m})^2. \quad (5.2)$$

For a typical 3-ion system the computational complexity is dominated by the number of phonon spaces in the problem and their required cutoff. When initial phonon population is large, simulating a complete set of phonon modes becomes impossible. In these cases we use smaller cutoff for phonon spaces with smaller change of in population or only consider near-resonance modes as discussed in section 4.6. The detailed approximation for each model will be discussed in section 6.

5.2 Quantum Time Evolution

The time-evolution of an open quantum system under Born-Markov approximation can be computed by solving the Lindbladian master equation[31][42]:

$$\frac{\partial \hat{\rho}}{\partial t} = \frac{1}{i} [\hat{H}, \hat{\rho}] + \hat{L}(\hat{\rho}), \quad (5.3)$$

$\hat{\rho}$ is the density matrix representation of quantum state and \hat{H} is the Hamiltonian of the system. Lindbladian super-operators \hat{L} describes the interaction between the system and an external environment. Eq. (5.3) is solved numerically with “Qutip: mesolve” which evolves the density matrix with 12-th order Adams–Bashforth method [43].

The time-evolution of a closed quantum system can be solved using the Schrödinger equation [31]:

$$i \frac{\partial}{\partial t} |\psi\rangle = \hat{H} |\psi\rangle, \quad (5.4)$$

$|\psi\rangle$ is the ket representation of the quantum state and \hat{H} is the Hamiltonian of the system. Eq. (5.4) is solved numerically via complete-diagonalization when \hat{H} is time-independent. Equation involving a time-dependent \hat{H} is solved by evolving the state vector in a similar way as for open quantum system case using “Qutip: sesolve”.

5.3 Energy Diagram

The Eigenenrgy diagram is an intuitive approach to understand the properties of donor-acceptor system in Eqs. (2.1),(2.5). Following the procedure in Ref. [30], we do a semi-classical approximation to phonon operators by replacing the phonon displacement operator with a real number and neglecting the momentum operator:

$$\hat{X} \rightarrow \frac{x_m}{X_{0m}} = x_{0m}, \quad \hat{P}^2 \rightarrow 0. \quad (5.5)$$

For the m th mode, $X_{0m} = \sqrt{\frac{1}{2m\omega_m}}$ is defined as the scale factor and x_{0m} is defined as the normalized displacement coordinate. We apply this approximation to the trapped-ion simulator Hamiltonian in Eq. (4.8):

$$\hat{H}_{sc} = E_1 \hat{\sigma}_1^z + E_2 \hat{\sigma}_2^z + J_{12} (\hat{\sigma}_1^+ \hat{\sigma}_2^- + h.c.) + \sum_{i=1}^2 \sum_{m=1}^3 \frac{\sqrt{2}\Omega_i \eta_{im}}{2} \hat{\sigma}_i^z x_{0m} - \sum_{m=1}^3 \frac{\delta_m}{2} (x_{0m}^2 - \hat{I}). \quad (5.6)$$

The above equation can be further simplified by mapping it to an equivalent one-site system following Eqs (2.5) and (2.6):

$$\begin{aligned} \hat{H}'_{sc} &= J_{12} \hat{\sigma}_x + (E_1 - E_2) \hat{\sigma}_z + \sum_{m=1}^3 \frac{\sqrt{2}}{2} (\Omega_1 \eta_{1m} - \Omega_2 \eta_{2m}) x_{0m} \hat{\sigma}_z - \sum_{m=1}^3 \frac{\delta_m}{2} (x_{0m}^2 - \hat{I}) \\ &= J_{12} \hat{\sigma}_x + \left[\frac{\Delta E}{2} + \sum_{m=1}^3 \frac{g_m}{2} x_{0m} \right] \hat{\sigma}_z - \sum_{m=1}^3 \frac{\delta_m}{2} (x_{0m}^2 - \hat{I}), \end{aligned} \quad (5.7)$$

where we define

$$g_m \equiv \sqrt{2}(\Omega_1 \eta_{1m} - \Omega_2 \eta_{2m}), \quad \Delta E = 2(E_1 - E_2). \quad (5.8)$$

For a specific mode $m = m'$ we can plot two eigenenergies of the system as a function of $x_{m'}$ while setting the displacements of the other 2 modes to 0. For a given $x_{m'}$, these eigenenergies are just the eigenvalues of a Hermitian operator:

$$\hat{H}'_{sc} = J_{12}\hat{\sigma}_x + \left[\frac{\Delta E}{2} + \frac{g_{m'}}{2}x_{0m'} \right] \hat{\sigma}_z - \frac{\delta_{m'}}{2} (x_{0m'}^2 - \hat{I}). \quad (5.9)$$

First consider the unperturbed case when $J_{12} = 0$, the eigenstates of the system is simply given by $|\uparrow\rangle, |\downarrow\rangle$ (or equivalently: $|\uparrow\downarrow\rangle, |\downarrow\uparrow\rangle$ for the two site system) and corresponding eigenenergies (note we always set $\delta_m < 0$ as discussed in section 4):

$$\begin{aligned} E &= \pm(\Delta E/2 + g_{m'}/2x_{0m'}) - \frac{\delta_{m'}}{2}x_{0m'}^2 + \frac{\delta_{m'}}{2} \\ &= \frac{|\delta_{m'}|}{2} \left(x_{0m'} \pm \frac{g_{m'}}{2|\delta_{m'}|} \right)^2 + \frac{1}{2} \left(\pm\Delta E + \delta_{m'} - \frac{g_{m'}^2}{2|\delta_{m'}|} \right). \end{aligned} \quad (5.10)$$

which are quadratic functions with minimums located at $\pm \frac{g_{m'}}{2|\delta_{m'}|}$. The energy difference between the two minimums is just ΔE . The general case can be solved numerically or analytically :

$$E = \pm \sqrt{\left(\frac{\Delta E}{2} + \frac{g_{m'}}{2}x_{0m'} \right)^2 + J_{12}^2} - \frac{\delta_{m'}}{2}x_{0m'}^2 + \frac{\delta_{m'}}{2}. \quad (5.11)$$

With $x_{m'} \rightarrow \pm\infty$, the effect of J_{12} becomes negligible so the eigenstates can be approximated as the unperturbed states. Hence we label the two curves in terms of unperturbed states according to their configuration in this limiting regime. The difference from unperturbed case only becomes significant near the intersection of two curves. With a non-zero J_{12} , the intersecting point turns into a avoided crossing as $\hat{\sigma}_x$ mixes the unperturbed eigenstates [31]. This mixing is essential for EET to take place as it couples the two eigenenergy curves.

After computing the eigenenergy curves, the harmonic energy levels of mode m' spaced by $|\delta_{m'}|$ can then be plotted on the energy diagram. Note the ground state energy level is located at $E = E_{min}$ instead of $E = E_{min} + |\delta_{m'}|/2$ because we have neglected the constant $\delta_m/2$ when writing the Hamiltonian.

5.4 Signatures of Quantum Chaos and Delocalization

Unlike classical chaos which has common features in terms of Lyapunov exponents [44], criterias and signatures of quantum chaos tends to vary for different types of systems. The first type of signature we will be using is based on the energy level clustering of a time-independent Hamiltonian [45]. For an integrable system, spacings of neighboring eigenenergy levels will follow an exponential distribution:

$$P(S) = \exp(-S). \quad (5.12)$$

which is often referred as Poissonian because the levels in this case has an analogy to random events in a Poissonian random process. For chaotic systems, the spacings follow more complicated Wiegner-Dyson distributions dervied from random matrix theory. The properties of level spacing distribution can be characterized by an energy level statistic r defined as [46]:

$$\langle r \rangle = \frac{1}{n} \sum_n \frac{\min(E_{n+1} - E_n, E_n - E_{n-1})}{\max(E_{n+1} - E_n, E_n - E_{n-1})}. \quad (5.13)$$

In general, $\langle r \rangle \rightarrow 0.39$ for a Poissonian system and $\langle r \rangle \rightarrow 0.53$ for a Wiegner-Dyson type system. The level clustering technique is independent of initial state but it only applies for systems with

a time-independent Hamiltonian. The other three type of signatures involve tracking the time evolution of some observables. By definition of quantum delocalization, the system will lose its memory of initial state in time evolution. Quantitatively we can define a dilution factor as the long-time average of survival probability [25]:

$$\sigma = \left\langle |\langle \psi(0) | \psi(t) \rangle|^2 \right\rangle_{t \rightarrow \infty}. \quad (5.14)$$

Here $\langle \rangle$ means the time average of variable inside. In this case $\sigma \rightarrow 0$ means the system completely loses its memory of initial state. However, the dilution factor is not experimentally favorable because we are not capable of measuring spin and phonon state population simultaneously and in numerical simulations we find it is not very useful in measuring delocalization in spin space.

For delocalization in spin space, it is convenient to study the evolution of spin imbalance observable \hat{L} [46]. Consider a tensor product space of N spin-1/2 states with M of them initialized as $|\uparrow\rangle$ with index j and $N - M$ of them initialized as $|\downarrow\rangle$ with index j' :

$$\hat{L}(t) = \frac{\sum_{j=1}^M \langle \hat{\sigma}_j^z(t) \rangle}{N} - \frac{\sum_{j'=1}^{N-M} \langle \hat{\sigma}_{j'}^z(t) \rangle}{N - M}. \quad (5.15)$$

As the spin space is initialized with $\hat{L}(0) = 2$, $L(t)$ would remain nearly unchanged for a localized case or evolve to $\hat{L}(t) = 0$ when the state becomes completely thermalized as a result of delocalization.

In comparison to classical cases, chaotic quantum systems are not sensitive to slightly different initial conditions because the overlap between two distinct states will be preserved by the unitary evolution operator. However, two identical initial states evolving under two slightly different Hamiltonians will result in diverging trajectories if the quantum system is chaotic ([45], [47]). Suppose the same initial states $|\psi_0\rangle$ are prepared for two systems with very similar Hamiltonians \hat{H}_1, \hat{H}_2 with corresponding unitary evolution operator \hat{U}_1, \hat{U}_2 , such features can be shown by computing:

$$\begin{aligned} \Delta P_\psi(t) &= |\langle \psi_1(t) | \psi_2(t) \rangle|^2, \\ \Delta A_\psi(t) &= \langle \psi_1(t) | \hat{A} | \psi_1(t) \rangle - \langle \psi_2(t) | \hat{A} | \psi_2(t) \rangle. \end{aligned} \quad (5.16)$$

where $|\psi_i(t)\rangle = \hat{U}_i(t) |\psi_0\rangle$, and \hat{A} is some observable we can choose.

Due to the lack of a common criteria and signatures for chaotic quantum systems, we will be using a combination of the above signatures to probe the existence of delocalization.

6 Results and Discussion

In this section we present the results for multiple trapped-ion setups based on the models discussed in section 2. For each setup we first simplify the Hamiltonian following the procedure described in section 5.1. These approximated forms will be used in numerical simulations.

6.1 Donor-Acceptor Pair: Trapped-ion Simulation

6.1.1 Hamiltonian under Approximation

As discussed in section 4.2, we numerically simulate Eq. (4.8) following a similar setup as in [30].

It is convenient to define an effective coupling coefficient to illustrate the magnitude of s-p (spin-phonon) coupling:

$$\Omega_{\text{eff}} = \Omega X_0 \Delta k, \quad (6.1)$$

where $X_0 \equiv \sqrt{1/2M\omega_x}$ is the harmonic oscillator length for radial COM mode. With this definition, we can rewrite s-p coupling between ion i and mode m as:

$$\Omega_{\zeta_{jm}} = \Omega_{\text{eff}} \frac{X_{0m}}{X_0} T_{jm} \sim \Omega_{\text{eff}}, \quad (6.2)$$

where T_{jm}, X_{0m} follow the same definition as in (3.22). For simplicity, we set Ω_j to be the same value for both ion 1 and ion 2. In this case, using Eq. (2.6), the COM mode will not contribute to the evolution since $\lambda_{11} - \lambda_{21} = 0$. We therefore exclude this mode from calculation.

The Hamiltonian used for simulation can be simplified to:

$$\hat{H} = \sum_{j=1}^2 E_j \hat{\sigma}_z^j + J_{12} (\hat{\sigma}_1^+ \hat{\sigma}_2^- + h.c.) + \sum_{j=1}^2 \frac{\Omega_{\text{eff}}}{2} \hat{\sigma}_j^z \sum_{m=2,3} \frac{X_{0m}}{X_0} T_{jm} (\hat{b}_m + \hat{b}_m^\dagger) - \sum_{m=2,3} \delta_m \hat{b}_m^\dagger \hat{b}_m, \quad (6.3)$$

and the Lindbladian can be written as:

$$\hat{L}(\hat{\rho}) = \sum_{m=2,3} |T_{3,m}| \gamma_m (1 + \bar{n}_m) \left(\hat{b}_m \hat{\rho} \hat{b}_m^\dagger - \frac{1}{2} [\hat{b}_m^\dagger \hat{b}_m, \hat{\rho}] \right) + |T_{3,m}| \gamma_m \bar{n}_m \left(\hat{b}_m^\dagger \hat{\rho} \hat{b}_m - \frac{1}{2} [\hat{b}_m \hat{b}_m^\dagger, \hat{\rho}] \right). \quad (6.4)$$

We choose the initial state as:

$$|\psi_0\rangle = |\uparrow\downarrow\rangle \otimes |\bar{n} = 0.01\rangle \otimes |\bar{n} = 0.01\rangle, \quad (6.5)$$

where the ion 1 is in up state, ion 2 is in down state, and the system is cooled to a near ground thermal state with average phonon number $\bar{n} = 0.01$ for both tilt and rocking phonon modes (see Appendix C). We use $f_x = 2$ MHz, $f_z = 1$ MHz for trap setup. The eigenfrequencies of the system are shown in Figure 7. For all plots we use J_{12} and define normalized time as $t_0 = tJ_{12}/2\pi$.

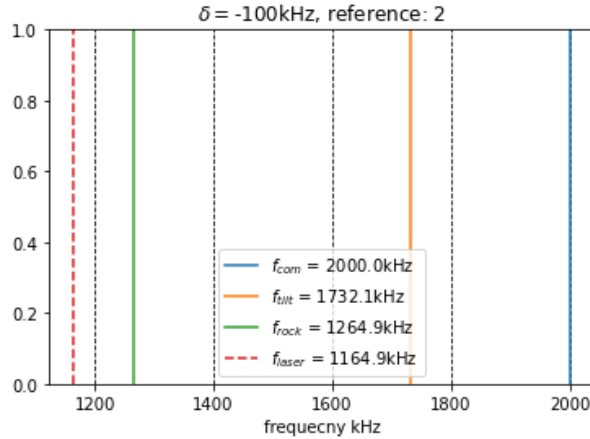


Figure 7: Radial eigenfrequencies of 3-ion system with $f_x = 2$ MHz, $f_z = 1$ MHz. From left to right are effective laser frequency μ (red dashed), rocking, tilt, COM mode frequencies, respectively.

6.1.2 Numerical results

We explore the conditions of resonant transfer in the near incoherent intermediate regime ($J_{12} \lesssim \gamma$). From the result in Ref. [30], we expect a similar mechanism: the transfer rate from ion 1 to ion 2 will be maximized when there is an overlap between harmonic energy levels. In the regime $J_{12} \ll \delta_r$, the difference between ground state energy level for the two eigenenergies curves is approximately ΔE as derived in section 5. Hence, the resonance condition is given by:

$$\Delta E = n\delta_r + m\delta_t \quad n, m \in \mathbb{N}^+. \quad (6.6)$$

Here we again use the notation δ_r , δ_t for rock mode and tilt mode detuning. With parameters in table 2 fixed, we simulate evolution of the spin population by at different site-energy difference ΔE .

Parameters	Values in [kHz]
Site-site coupling J_{12}	$2\pi \times 1$
Effective s-p coupling Ω_{eff}	$2\pi \times 50$
Detuning from ω_{rock} δ_r	$-2\pi \times 100$
Dissipation rate γ	$2\pi \times 10$

Table 2: Approximate parameter values used for simulating two-site Donor-Acceptor system

The spin/phonon evolution of a typical transfer is shown in Figure 8. The probability of observing the spin state $|\uparrow\downarrow\rangle$ is defined as:

$$P_{\uparrow\downarrow} = \text{Tr}(\hat{\rho}(t) |\uparrow\downarrow\rangle \langle\uparrow\downarrow|) \quad (6.7)$$

Figure 8 shows that $P_{\uparrow\downarrow}$ can be fitted by a exponential decay in form $A \exp(-kt) + B$ after neglecting the first few data points ($t_0 < 0.1$ in this case, for instance) and we extract k as the decay rate with normalized unit t_0^{-1} .

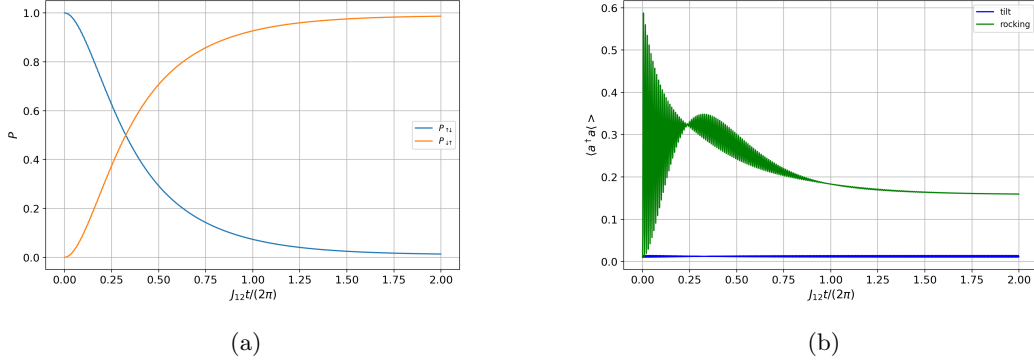


Figure 8: Dynamics of Donor-acceptor system at resonant transfer condition ($\Delta E = 2\pi \times 100$ kHz) with dissipation applied only on rocking mode and phonon cutoff [5, 10] for [tilt, rock] modes. **a)** evolution of spin population with initial state $|\uparrow\downarrow\rangle$ occupation in blue and transferred state $|\downarrow\uparrow\rangle$ in orange. **b)** evolution of phonon populations of tilt and rocking mode.

Three typical types of resonance are shown in Figure 9 ($[n = 1, m = 0]$), Figure 10 ($[n = 1, m = 0]$), Figure 11 ($[n = 1, m = 1]$), with energy diagram computed according to section 5.

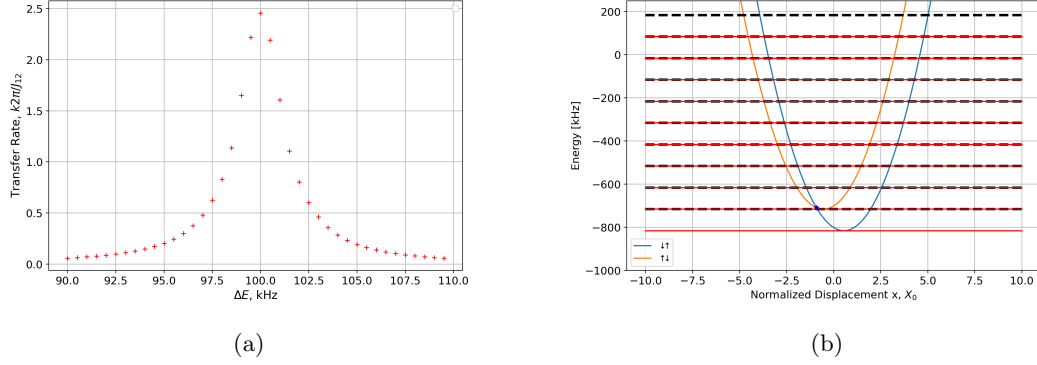


Figure 9: Resonance caused by the overlap between rocking mode energy levels. **(a)** Transfer rates k near the first resonance ($\Delta E/2\pi = |\delta_{rock}|/2\pi = 567.1$ kHz) as a function of energy splitting ΔE , with sample points spacing of 0.5 kHz. The maximum transfer rate takes place at $\Delta E/2\pi = 100$ kHz. **(b)** Energy diagram of the system at $\Delta E/2\pi = 100$ kHz Eigenenergy curves for the unperturbed eigenstates $|\uparrow\downarrow\rangle$ (orange), $|\downarrow\uparrow\rangle$ (blue) are plotted with corresponding rock mode harmonic energy levels. Energy spacing between two ground states is calculated to be 100.01 kHz theoretically. The simulation is done with dissipation applied only on rocking mode and phonon cutoff [5, 10] for [tilt,rock] modes and $P_{err} \lesssim 10^{-8}$.

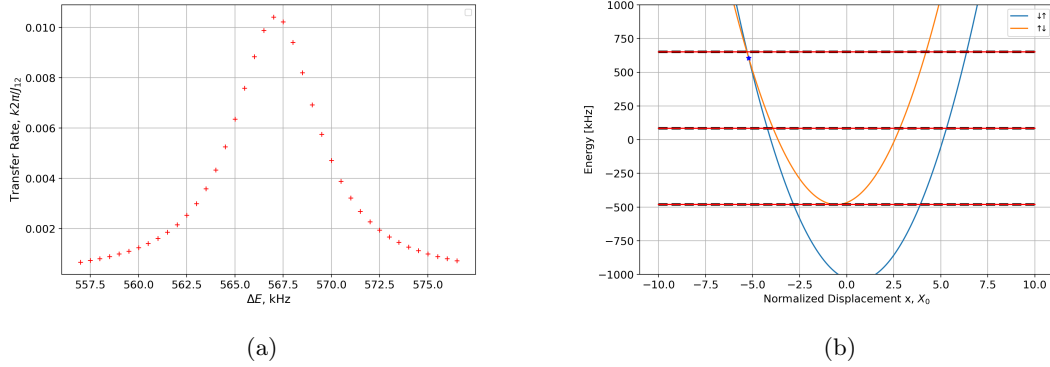


Figure 10: Resonance caused by the overlap between tilt mode energy levels. **(a)** Transfer rates k near the first resonance ($\Delta E = 1 \times |\delta_{tilt}| = 567.1$ kHz) as a function of energy splitting ΔE , with sample points spacing of 0.5 kHz. The maximum transfer rate takes place at $\Delta E/2\pi = 567$ kHz. **(b)** Energy diagram of the system at $\Delta E/2\pi = 567$ kHz Eigenenergy curves for the unperturbed eigenstates $|\uparrow\downarrow\rangle$ (orange), $|\downarrow\uparrow\rangle$ (blue) are plotted with corresponding tilt mode harmonic energy levels. Energy spacing between two ground states is calculated to be 567.00 kHz theoretically. The simulation is done with dissipation applied only on rocking mode and phonon cutoff [5, 10] for [tilt,rock] modes and $P_{err} \lesssim 10^{-8}$.

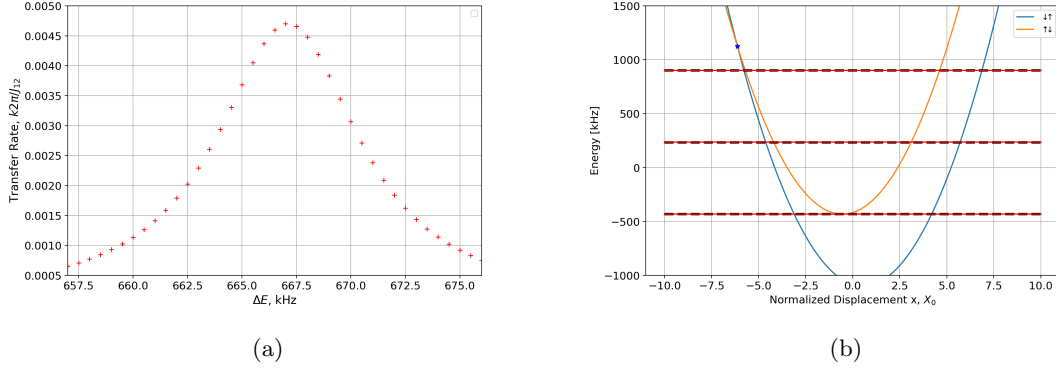


Figure 11: Resonance caused by the overlap between combinations of tilt and rocking mode energy levels. **(a)** Transfer rates k near the first resonance ($\Delta E = 1 \times |\delta_{\text{tilt}} + \delta_{\text{rock}}| = 667.1$ kHz) as a function of energy splitting ΔE , with sample points spacing of 0.5 kHz. The maximum transfer rate takes place at $\Delta E/2\pi = 667$ kHz. **(b)** Energy diagram of the system at $\Delta E/2\pi = 667$ kHz Eigenenergy curves for the unperturbed eigenstates $|\uparrow\downarrow\rangle$ (orange), $|\downarrow\uparrow\rangle$ (blue) are plotted with corresponding tilt+rocking mode harmonic energy levels. Energy spacing between two ground states is calculated to be 667.00 kHz theoretically. The simulation is done with dissipation applied on both tilt, rocking mode and phonon cutoff [5, 10] for [tilt,rock] modes and $P_{\text{err}} \lesssim 10^{-8}$.

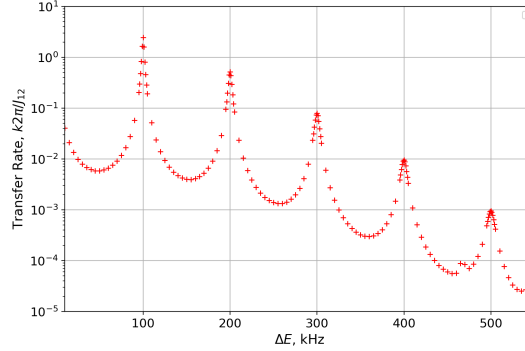


Figure 12: Transfer rate k in log scale as a function of energy splitting ΔE for type 1 resonance sample points spacing of 1 kHz near resonance point $\Delta E/2\pi = n|\delta_m|$ and 10 kHz in off-resonance regime to track the general shape. The simulation is done with dissipation applied only on rocking mode and phonon cutoff [5, 15] for [tilt,rock] modes and $P_{\text{err}} \lesssim 10^{-10}$.

We also test the dependence of resonant transfer rate on γ . Although the normalization of transfer rate is problematic, the general trend is consistent with Ref. [30] (see Appendix D).

6.1.3 Discussion

The simulation results obtained are in agreement with those of a one-site system comprising a single set of phonon modes studied in Ref. [30]. Theoretically the resonance condition in Eq.

(6.2) is consistent with the prediction of Forster resonant transfer model [11]:

$$k = 2\pi|V|^2 \sum_{\nu,\nu'} p_{\nu'} FC_{\nu,\nu'} \delta(E_{D,\nu} - E_{A,\nu'}), \quad (6.8)$$

$E_{D,\nu}, E_{A,\nu'}$ are the eigenenergy of donor phonon eigenstate $|\uparrow\downarrow\rangle \otimes |\nu\rangle$ and acceptor phonon eigenstate $|\downarrow\uparrow\rangle \otimes |\nu'\rangle$ for harmonic energy level index ν, ν' , p_{ν} describe the initial thermally distributed phonon populations, $FC_{\nu,\nu'}$ is the Franck-Condon factor between harmonic energy level index ν, ν' . The actual transfer rate is determined by $FC_{\nu,\nu'}$ and dissipation rate γ . The latter also causes the broadening of the peaks. In the regime where $V \gg J_{12}$, such effects will be more significant, resulting in a nearly continuous “spectrum” of $k(\Delta E)$. This will be a interesting regime for further research. It may be feasible to tune the parameters carefully and establish a nearly linear relation between k and ΔE . Overall, this consistency with the Forster resonant transfer model serves as a benchmark for both the numerical methods and computational modules we have employed so far in our study.

Furthermore, our system is more realistic due to its coupling to multiple sets of intermolecular modes, which provides a richer set of resonant conditions. This will make the experimental realization of continuous transfer rate spectrum easier.

Our system is also capable of simulating intramolecular vibrations. Instead of being coupled to the same set of phonon modes, each site will have vibrational motions independent of the other sites. Using individual addressing, we will be capable of coupling the donor and acceptor sites to two independent but identical sets of radial motional modes. We can further expand our capability of AQS based on this prototype simulator by scaling up the number of ions and simulate more complicated EET models such as the one in Ref. [18].

6.2 Anharmonicity Induced Delocalization

In this subsection we present numerical results for anharmonicity induced delocalization in three different setups of simulators as discussed in section 4. First we want to validate that the allowed parameter space is capable of generating delocalization. Based on that, we further examine if the simultaneous presence of spin phonon coupling and anharmonic coupling interactions in these systems can cause the transition to chaotic regime. We start by specifying the parameters to be used for simulation, we illustrate a general procedure for probing quantum chaos and then we discuss the results in detail.

6.2.1 Parameter Space and Simulation Procedure

The trap radial confining frequency is set to $f_x = 3.1$ MHz, while axial confining frequency is determined by desired the anharmonic detuning δ_{ah} using (4.15). We apply a similar set of parameters as in Ref. [25]. The definition of these parameters and their values are listed in Table 3. We choose rocking mode detuning as energy scale: $\delta_0 = |\delta_r|$. Again we define normalized time as:

$$t_0 = t\delta_0/2\pi \quad (6.9)$$

Parameters	Values in [kHz]
Energy Scale: δ_0	$2\pi \times 80$
Site-energy Splitting: ΔE	$2\delta_0$
Site-energy coupling: Ω_x	$0.3\delta_0$
Effective s-p coupling: Ω_{eff}	$\lesssim 0.5\delta_0$
Resonant anharmonic coupling: C_{ah}	$\lesssim 0.05\delta_0$
Detuning from Radial rocking: $\omega_r \delta_r$	$-\delta_0$
Detuning from Axial tilt: $\nu_t \delta_t$	$-2\delta_0$

Table 3: Definition and values of parameters used for simulating anharmonic induced delocalization.

For all three setups, the existence of delocalization and the contribution from different terms are tested according to the following general procedure.

- We first test the effects of spin-phonon coupling strength on the system's behavior by varying Ω_{eff} from $0.1\delta_0$ to δ_0 with all other parameters fixed and anharmonicity at resonance. As an initial probe, for each value we compute the energy level statistic $\langle r \rangle$ using Eq. (5.13) in the resonant frame.
- We simulate the time evolution by numerically solving Eq. (5.4) in ordinary frame for state $\psi(t)$ and compute the value of a spin observable $\langle A(t) \rangle$.
- Then we slightly vary the parameters in H by increasing Ω_{eff} with 1% and solve for state $|\psi'(t)\rangle$ and observable $\langle A'(t) \rangle$. Following the procedure in section 5, we investigate the time evolution of $\Delta P_\psi(t)$ and $\Delta L_\psi(t)$ as defined in Eq. (5.16) for chaotic signatures

The effects of anharmonic coupling can be tested in the same way. In this case we fix the ratio between all other parameters and decrease the effect of anharmonic term by increasing δ_{ah} to detune away from resonant anharmonicity. Note δ_{ah} is implicitly tuned via trap frequency, whose changes will also modulate the value of C_{ah} . Therefore, we need to change δ_0 accordingly to make sure $\delta_{ah}/\delta_0 \sim 0.05$ is still valid. Values of δ_0 for a given δ_{ah} are listed in Table 4.

Energy Scale: δ_0 [kHz]	Anharmonic detuning: $\delta_{ah} [\delta_0]$
$2\pi \times 80$	0
$2\pi \times 83$	-1
$2\pi \times 95$	-5

Table 4: Energy scale and anharmonic detuning to be used for testing the effect of anharmonic coupling.

6.2.2 Two-drive configuration: Hamiltonian under Approximation

Following sections 4.3 and 4.4, we create Fermi-resonant coupling between axial tilt and radial rocking mode by tuning the trap frequency and setting the effective laser frequency μ_1, μ_2 such that resonant condition $2\omega_r = \omega_t$ and $2\mu_2 = \mu_1$ are satisfied simultaneously, or in terms of detuning:

$$2\omega_r = \omega_t, \quad 2\delta_r = \delta_t. \quad (6.10)$$

To probe the existence of chaotic behavior, it is necessary to start from a relatively highly excited phonon state and we have to use a large cutoff for the phonon-space. To make the computational complexity approachable for our numerical method, we use small detunings from axial tilt (phonon operator \hat{a}_t) and radial rocking (phonon operator \hat{b}_r) mode. This way we can

neglect the far-detuned motional modes that are also far from the anharmonic resonance. The Hamiltonian in Eq. (4.22) can be approximated as:

$$\begin{aligned}
\hat{H}_{res} = & \frac{\Delta E}{2} \sum_j \sigma_z^{(j)} + V \sum_j \sigma_x^{(j)} \\
& + \frac{1}{2} \sum_j \Omega_{eff,r} \frac{X_{r0}}{X_0} T_{jr} \sigma_z^{(j)} (\hat{b}_r + \hat{b}_r^\dagger) + \frac{1}{2} \sum_j \Omega_{eff,t} \frac{X_{t0}}{X_0} T_{jt} \sigma_z^{(j)} (\hat{a}_t + \hat{a}_t^\dagger) \\
& - \delta_r \hat{b}_r^\dagger \hat{b}_r - \delta_t \hat{a}_t^\dagger \hat{a}_t + C_{ah} \hat{a}_t^\dagger \hat{b}_r \hat{b}_r + C_{ah} \hat{a}_t \hat{b}_r^\dagger \hat{b}_r^\dagger.
\end{aligned} \tag{6.11}$$

To test the effect of anharmonic coupling, the trap frequency is detuned away from resonance. It is convenient to simulate in the ordinary frame, as discussed in section 4.6. The approximated Hamiltonian can be derived from Eqs. (3.37) and (4.18) as:

$$\begin{aligned}
\hat{H}_{ord} = & \frac{\Delta E}{2} \sum_j \hat{\sigma}_z^j + V_t \sum_j \hat{\sigma}_x^j \\
& + \sum_j \Omega_{eff,t} \frac{X_{t0}}{X_0} \hat{\sigma}_z^j T_{tr} \cos(\mu_1 t) \left(\hat{a}_t e^{-i\omega_t t} + \hat{a}_t^\dagger e^{i\omega_t t} \right) \\
& + \sum_j \Omega_{eff,r} \frac{X_{r0}}{X_0} \hat{\sigma}_z^j T_{jr} \cos(\mu_2 t) \left(\hat{b}_r e^{-i\omega_r t} + \hat{b}_r^\dagger e^{i\omega_r t} \right) \\
& + C_{ah} \left[\left(2\hat{a}_t \hat{b}_r^\dagger \hat{b}_r e^{-i\omega_t t} + \hat{a}_t \hat{b}_r^\dagger \hat{b}_r^\dagger e^{i\delta_{ah} t} \right) + \text{h.c.} \right],
\end{aligned} \tag{6.12}$$

where $\delta_{ah} = 2\omega_r - \omega_t$ is the effective anharmonic detuning.

6.2.3 Two-drive configuration with one site: Numerical Results

By only allowing ion index $j = 1$ for the two drives configuration, a 1-site system that has a similar structure as Eq. (2.7) can be obtained.

We follow the procedure in section 6.2.1 with initial state $|\psi_0\rangle = |\downarrow\rangle \otimes |n=5\rangle \otimes |n=5\rangle$. Since there is only 1 spin space, $\langle L \rangle$ is not defined. Hence, we only use time evolution under slightly different \hat{H} as a signature and choose $\hat{A} = \hat{\sigma}_z$ for $\Delta A_\psi(t)$. The results of the level statistics $\langle r \rangle$ and the spin observables for Ω_{eff} are shown in Figure 13 and 14 and the results for anharmonic coupling are shown in Figure 15.

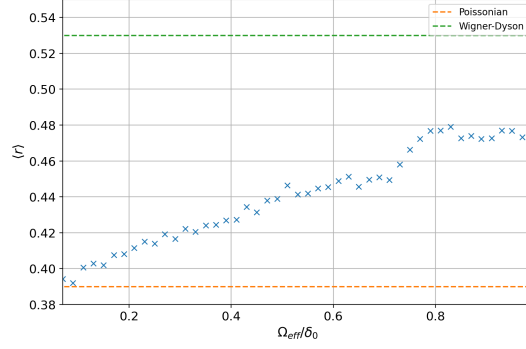


Figure 13: Energy level statistic $\langle r \rangle$ as a function of effective Rabi frequency $\Omega_{\text{eff}}/\delta_0$ (blue). The dashed lines are the criterion for integrable/chaotic systems $\langle r \rangle = 0.39, \langle r \rangle = 0.53$, respectively. $\langle r \rangle$ continues to increase in the plotted regime. Further increasing Ω requires a larger phonon cutoff since phonon excitation also increases.

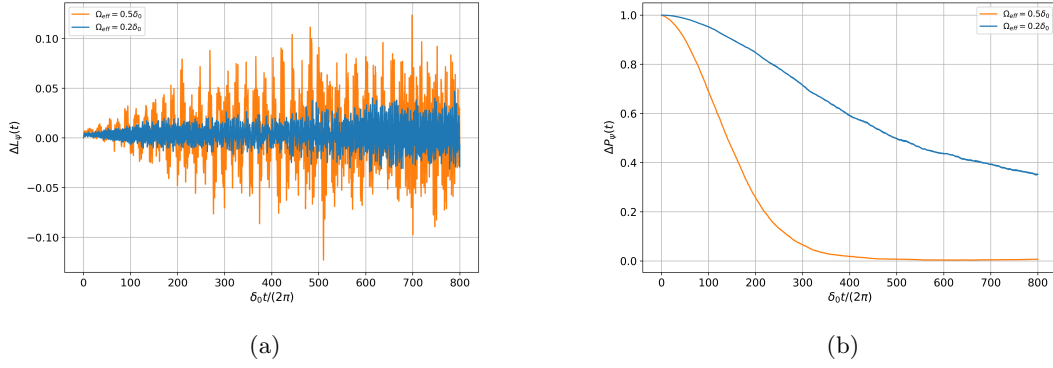


Figure 14: Chaotic signatures due to spin-phonon coupling probed using slightly different Hamiltonian for a two-drive, one-site system initialized as $|\downarrow\rangle$. Anharmonic term is set to resonance and $\Omega_{\text{eff}} = 0.5\delta_0$ (blue), $\Omega_{\text{eff}} = 0.2\delta_0$ (orange). **(a)** Evolution of difference in spin imbalance observable, $\Delta L_\psi(t)$ **(b)** Evolution of the overlap between two identical initial states, $\Delta P_\psi(t)$. With $\Omega_{\text{eff}} = 0.5\delta_0$, the difference between observable values increases fast and saturates at a relatively large value ~ 0.1 in comparison to $\Omega_{\text{eff}} = 0.2\delta_0$ case, indicating a more chaotic behavior for large Ω_{eff} . The overlap between two identical initial states shows a result with similar interpretations. The simulation is done with phonon cutoff $[60, 60]$ for [tilt, rock] modes and $P_{\text{err}} \lesssim 10^{-40}$.

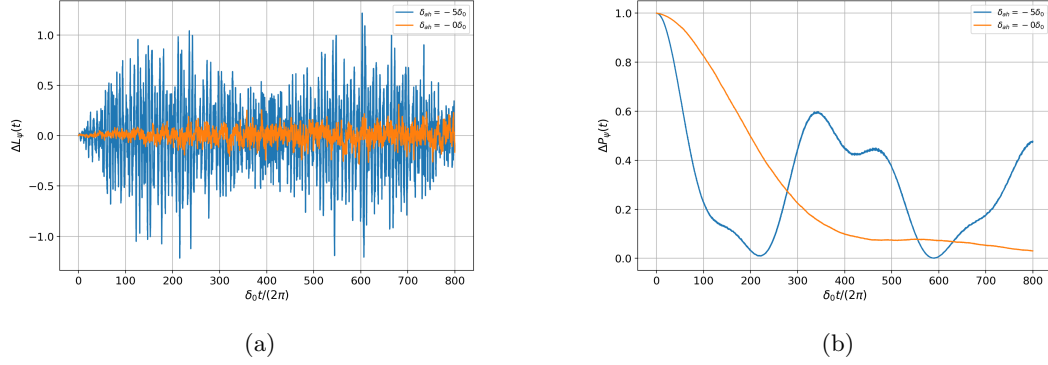


Figure 15: Chaotic signatures probed using slightly different Hamiltonian for a two-drive, one-site system initialized as $|\downarrow\rangle$, with Ω_{eff} fixed at $0.4\delta_0$ and $\delta_{ah} = 0$ (orange), $\delta_{ah} = -5\delta_0$ (blue) **(a)** Evolution of difference in spin observable $\Delta\sigma_{z,\psi}(t)$ **(b)** Evolution of the overlap between two identical initial states, $\Delta P_\psi(t)$. With resonant anharmonicity, the difference between observable values increases after time and saturates at a small finite value ~ 0.25 . With near zero effective anharmonic coupling (large δ_{ah}), the difference between these observables increases very fast to about 1 but then bounces back to ~ 0.5 , again showing a quasi-periodic behavior. The overlap between two identical initial states shows a result with similar interpretations. The simulation is done with phonon cutoff $[50, 50]$ for [tilt, rock] modes and $P_{\text{err}} \lesssim 10^{-20}$.

6.2.4 Two-drive configuration with multiple Sites: Numerical Results

By allowing ion index $j = 1, 2, 3$ for one-drive configuration, a three-site system that has a similar structure as Eq. (2.8) can be obtained. We follow the procedure in section 6.2.1 with initial state $|\psi_0\rangle = |\downarrow\uparrow\downarrow\rangle \otimes |n=5\rangle \otimes |n=5\rangle$. We choose $\hat{A} = \hat{L}$ for $\langle\hat{A}\rangle$. The results for Ω_{eff} are shown in Figure 16, 17a, 18 and the results for anharmonic coupling are shown in Figure 17b, 19.

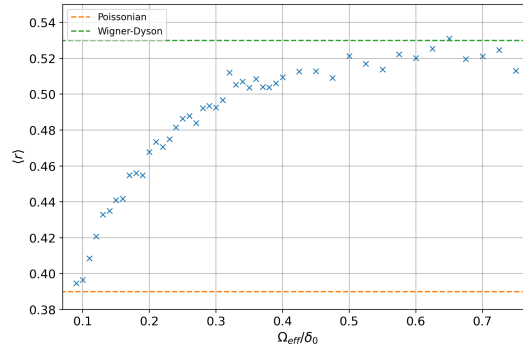


Figure 16: Energy level statistic $\langle r \rangle$ as a function of effective Rabi frequency $\Omega_{\text{eff}}/\delta_0$ (blue). The dashed lines are the criterion for integrable/chaotic systems $\langle r \rangle = 0.39$, $\langle r \rangle = 0.53$, respectively. $\langle r \rangle$ saturates at ~ 0.53 at $\Omega \sim 0.6\delta_0$ indicating a chaotic behavior.

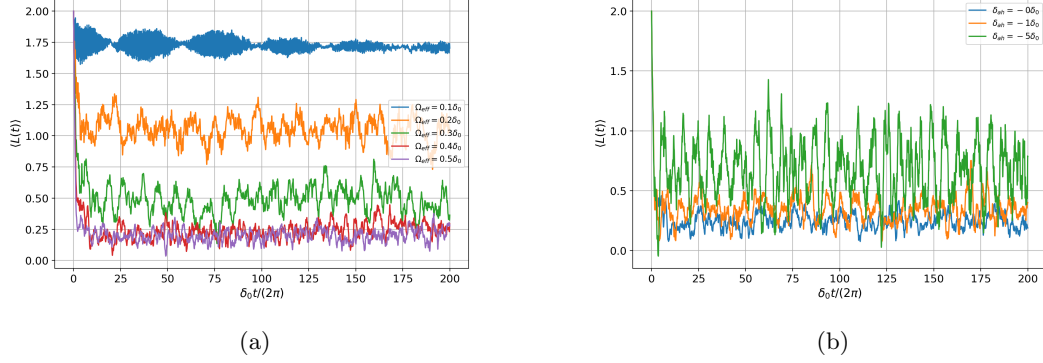


Figure 17: Time evolution of spin imbalance observable. $\langle L(t) \rangle$ for a two-drive, three-site system initialized as $|\downarrow\uparrow\downarrow\rangle$ (a) $\langle L(t) \rangle$ with spin-phonon coupling $\Omega_{\text{eff}} = 0.1\delta_0, 0.2\delta_0, 0.3\delta_0, 0.4\delta_0, 0.5\delta_0$ and resonance anharmonic coupling. With Ω_{eff} increasing, $\langle L(t) \rangle$ approaches 0 in the long term, indicating a clear transition from integrable to chaotic behavior. (b) $\langle L(t) \rangle$ with anharmonic detuning $\delta_{ah} = 0, -1\delta_0, -5\delta_0$ and $\Omega_{\text{eff}} = 0.4\delta_0$. As effective anharmonic coupling strength decreases, $\langle L(t) \rangle$ deviates from 0 but also shows a feature quasi-periodic feature with increasing amplitudes of oscillation. The simulation is done with phonon cutoff $[20, 40]$ for [tilt,rock] modes and $P_{\text{err}} \lesssim 10^{-11}$.

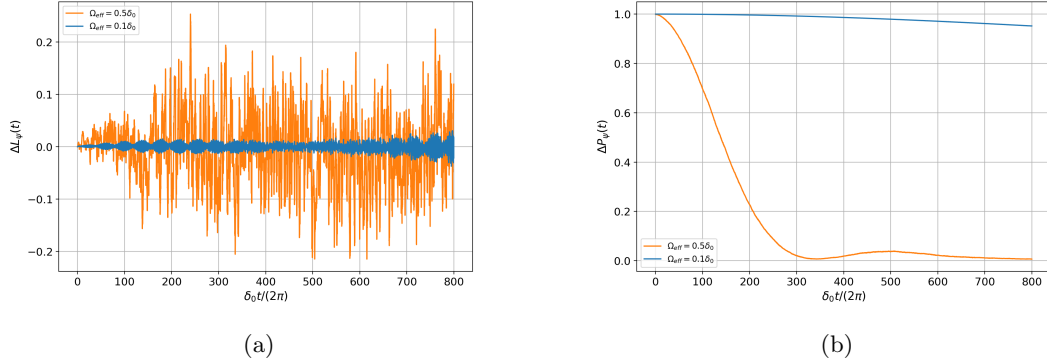


Figure 18: Chaotic signatures due to spin-phonon coupling probed using slightly different Hamiltonian for a two-drive, three-site system initialized as $|\downarrow\rangle$. Anharmonic term is set to resonance and $\Omega_{\text{eff}} = 0.5\delta_0$ (blue), $\Omega_{\text{eff}} = 0.1\delta_0$ (orange). (a) Evolution of difference in spin imbalance observable, $\Delta L_\psi(t)$ (b) Evolution of the overlap between two identical initial states, $\Delta P_\psi(t)$ with Hamiltonians with Ω_{eff} differing by 1%. With $\Omega_{\text{eff}} = 0.5\delta_0$, the difference between observable values increases fast and saturates at a relatively large value ~ 0.25 in comparison to $\Omega_{\text{eff}} = 0.1\delta_0$ case, indicating a more chaotic behavior for large Ω_{eff} . The overlap between two identical initial states shows a result with similar interpretations. The simulation is done with phonon cutoff $[20, 40]$ for [tilt,rock] modes and $P_{\text{err}} \lesssim 10^{-11}$.

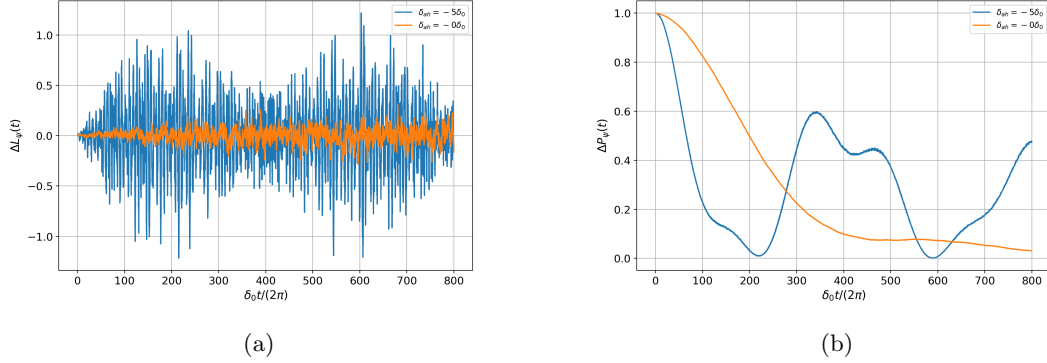


Figure 19: Chaotic signatures probed using slightly different Hamiltonian for a two-drive, three-site system initialized as $|\downarrow\uparrow\downarrow\rangle$, with Ω_{eff} fixed at $0.4\delta_0$ and $\delta_{ah} = 0$ (orange), $\delta_{ah} = -5\delta_0$ (blue) **(a)** Evolution of difference in spin imbalance observable $\Delta L_\psi(t)$ **(b)** Evolution of the overlap between two identical initial states, $\Delta P_\psi(t)$ with Hamiltonians with Ω_{eff} differing by 1%. With resonant anharmonicity, the difference between observable values increases after time and saturates at a small finite value ~ 0.25 . With near zero effective anharmonic coupling (large δ_{ah}), the difference between these observables increases very fast to about 1 but then bounces back to ~ 0.5 , again showing a quasi-periodic behavior. The overlap between two identical initial states shows a result with similar interpretations. The simulation is done with phonon cutoff $[20, 40]$ for [tilt,rock] modes and $P_{\text{err}} \lesssim 10^{-11}$.

6.2.5 One-drive configuration: Hamiltonian under Approximation

In this section we will explore the delocalization phenomenology with only one drive, following the discussion in sections 4.3 and 4.5. This configuration has a Hamiltonian of similar structure as the two-drive configuration and it is more experimentally favorable since it only requires applying sideband drives in radial direction, which is within the capability of our current lab setup. First let us consider the case where anharmonic term is on resonance. Applying a similar approximation as for two-drive configuration to Eq. (4.24), the Hamiltonian in resonant frame can be approximated as:

$$\begin{aligned} \hat{H}_{\text{res}} = & \frac{\Delta E}{2} \sum_j \sigma_z^{(j)} + V \sum_j \sigma_x^{(j)} + \frac{1}{2} \sum_j \Omega_{\text{eff},r} \frac{X_{r0}}{X_0} T_{jr} \sigma_z^{(j)} (\hat{b}_r + \hat{b}_r^\dagger) \\ & - \delta \hat{b}_r^\dagger \hat{b}_r - 2\delta \hat{a}_t^\dagger \hat{a}_t + C_{ah} \hat{a}_t^\dagger \hat{b}_r \hat{b}_r + C_{ah} \hat{a}_t \hat{b}_r^\dagger \hat{b}_r^\dagger. \end{aligned} \quad (6.13)$$

Again we consider deviating from resonant anharmonicity in ordinary frame. In this case, it is still possible to have an equivalent time-independent Hamiltonian in resonant frame without changing the detuning δ . To keep $e^{i\delta_{ah}t}$ as the slowest process, we further require $\delta_{ah} < 0$ while $\delta, \Delta < 0$ for the resonant frame Hamiltonian to be physically meaningful. Rewrite $\delta = -\delta_0$, $\Delta = -\Delta_0$ where $\delta_0, \Delta_0 > 0$, the constraints for Δ_0 is given by:

$$\begin{aligned} 2\mu = \Lambda_t, \rightarrow 2(\omega_r + \delta_r) &= \nu_t + \Delta_t, \\ \delta_{ah} = 2\omega_r - \nu_t &< 0. \end{aligned} \quad (6.14)$$

which simplifies to

$$\Delta_0 > 2\delta_0. \quad (6.15)$$

We are free to adjust the parameter Δ introduced in Eq. (4.23) as it is purely mathematical so the above condition can always be satisfied.

Under these conditions, the time-independent Hamiltonian in resonant frame becomes:

$$\begin{aligned}\hat{H}_{res} = & \frac{\Delta E}{2} \sum_j \sigma_z^{(j)} + V \sum_j \sigma_x^{(j)} + \frac{1}{2} \sum_j \Omega_{eff,r} \frac{X_{r0}}{X_0} T_{jr} \sigma_z^{(j)} (\hat{b}_r + \hat{b}_r^\dagger) \\ & + \delta_0 \hat{b}_r^\dagger \hat{b}_r + \Delta_0 \hat{a}_t^\dagger \hat{a}_t + C_{ah} \hat{a}_t^\dagger \hat{b}_r \hat{b}_r + C_{ah} \hat{a}_t \hat{b}_r^\dagger \hat{b}_r^\dagger.\end{aligned}\quad (6.16)$$

With an equivalent Hamiltonian in ordinary frame:

$$\begin{aligned}\hat{H}_{ord} = & \sum_j \Omega_{eff,r} \frac{X_{r0}}{X_0} \hat{\sigma}_z^j T_{jr} \cos(\mu_r) \left(\hat{b}_r e^{-i\omega_r t} + \hat{b}_r^\dagger e^{i\omega_r t} \right) \\ & + C_{ah} \left[\left(2\hat{a}_t \hat{b}_r^\dagger \hat{b}_r e^{-i\nu_r t} + \hat{a}_t \hat{b}_r^\dagger \hat{b}_r^\dagger e^{i(2\delta_0 - \Delta_0)t} \right) + h.c. \right].\end{aligned}\quad (6.17)$$

here we write δ_{ah} in terms of detuning:

$$\delta_{ah} = 2\delta_0 - \Delta_0. \quad (6.18)$$

In simulation we first choose δ_{ah} and f_x . The axial trap frequency f_z can be determined by Eq. (4.15) and corresponding Δ determined by (6.18).

6.2.6 One-drive system: Numerical Results

By allowing ion index $j = 1, 2, 3$ for one-drives configuration, a three-site system that has a similar structure as Eq. (2.8) can be obtained.

We follow the procedure in section 6.2.1 with initial state $|\psi_0\rangle = |\downarrow\downarrow\downarrow\rangle \otimes |n=5\rangle \otimes |n=5\rangle$. We choose $\hat{A} = \hat{L}$ for $\langle \hat{A} \rangle$. The results for Ω_{eff} are shown in Figure 16, 17a, 18 and the results for anharmonic coupling are shown in Figure 17b, 19.

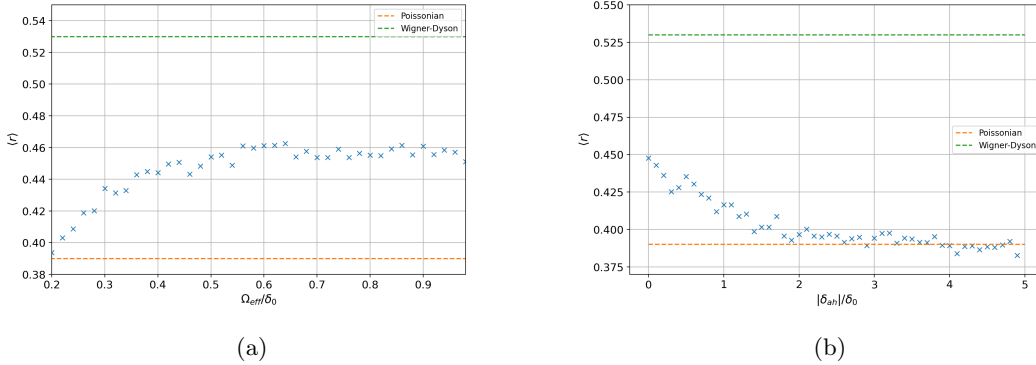


Figure 20: Plot of energy level statistic $\langle r \rangle$. The dashed lines are the criterion for integrable/chaotic systems $\langle r \rangle = 0.39, \langle r \rangle = 0.53$, respectively. **(a)** $\langle r \rangle$ as a function of effective Rabi frequency Ω_{eff}/δ_0 (blue). $\langle r \rangle$ saturates at ~ 0.46 at $\Omega \sim 0.6\delta_0$. **(b)** $\langle r \rangle$ as a function of anharmonic detuning $|\delta_{ah}|/\delta_0$ (blue). $\langle r \rangle$ drops back to 0.39 with a decrease in effective anharmonic coupling.

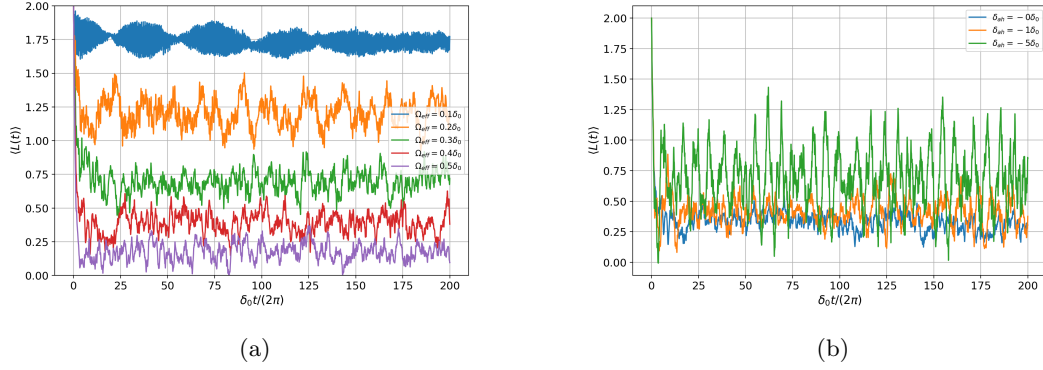


Figure 21: Spin imbalance observable $\langle L(t) \rangle$ for a one-drive, three-site system initialized as $|\downarrow\uparrow\downarrow\rangle$ (a) $\langle L(t) \rangle$ with spin-phonon coupling $\Omega_{\text{eff}} = 0.1\delta_0, 0.2\delta_0, 0.3\delta_0, 0.4\delta_0, 0.5\delta_0$ and resonance anharmonic coupling. With Ω_{eff} increasing, $\langle L(t) \rangle$ approaches 0 in the long term, indicating a clear transition from integrable to chaotic behavior. (b) $\langle L(t) \rangle$ with anharmonic detuning $\delta_{ah} = 0, -1\delta_0, -5\delta_0$ and $\Omega_{\text{eff}} = 0.4\delta_0$. As effective anharmonic coupling strength decreases, $\langle L(t) \rangle$ deviates from 0 but also shows a feature cutoff [20, 40] for [tilt, rock] modes and $P_{\text{err}} \lesssim 10^{-11}$. The simulation is done with phonon cutoff [20, 40] for [tilt, rock] modes and $P_{\text{err}} \lesssim 10^{-11}$.

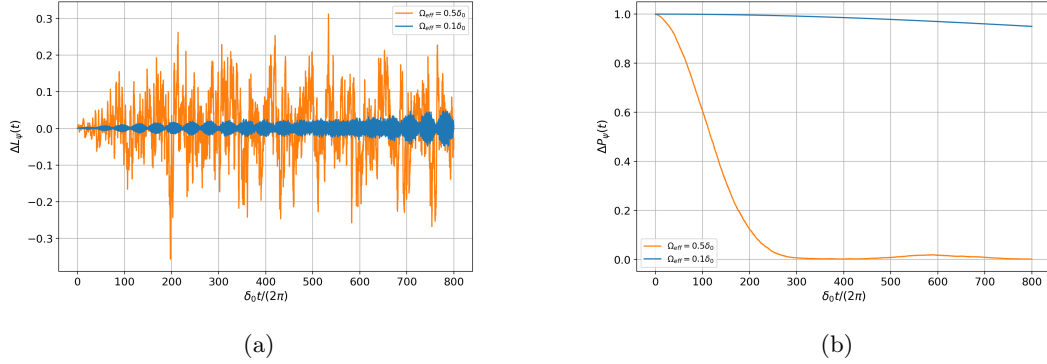


Figure 22: Chaotic signatures due to spin-phonon coupling probed using slightly different Hamiltonian for a one-drive, three-site system initialized as $|\downarrow\uparrow\downarrow\rangle$. Anharmonic term is set to resonance and $\Omega_{\text{eff}} = 0.5\delta_0$ (blue), $\Omega_{\text{eff}} = 0.1\delta_0$ (orange). (a) Evolution of difference in spin imbalance observable, $\Delta L_\psi(t)$. With $\Omega_{\text{eff}} = 0.5\delta_0$, the difference between observable values increases fast and saturates at a relatively large value ~ 0.25 in comparison to $\Omega_{\text{eff}} = 0.1\delta_0$ case, indicating a more chaotic behavior for large Ω_{eff} . (b) Evolution of the overlap between two identical initial states, $\Delta P_\psi(t)$ with Hamiltonians with Ω_{eff} differing by 1%. The overlap between two identical initial states shows a result with similar interpretations. The simulation is done with phonon cutoff [20, 40] for [tilt, rock] modes and $P_{\text{err}} \lesssim 10^{-11}$.

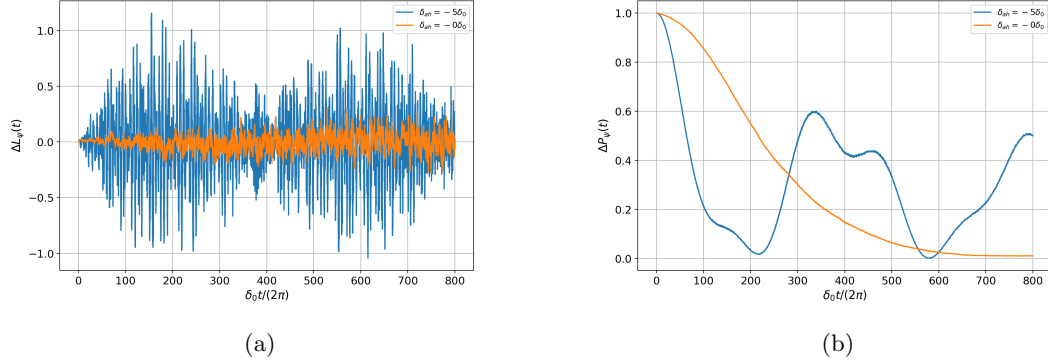


Figure 23: Chaotic signatures probed using two slightly different Hamiltonians for a one-drive, three-site system initialized as $|\downarrow\uparrow\downarrow\rangle$, with Ω_{eff} fixed at $0.4\delta_0$ and $\delta_{ah} = 0$ (orange), $\delta_{ah} = -5\delta_0$ (blue) (a) Evolution of difference in spin imbalance observable $\Delta L_\psi(t)$. With resonant anharmonicity ($\delta_{ah} = 0$), the difference between observable values increases after time and saturates at a small finite value ~ 0.25 . (b) Evolution of the overlap between two identical initial states, $\Delta P_\psi(t)$ with Hamiltonians with Ω_{eff} differing by 1%. With near zero effective anharmonic coupling (large δ_{ah}), the difference between these observables increases very fast to about 1 but then bounces back to ~ 0.5 , again showing a quasi-periodic behavior. The overlap between two identical initial states shows a result with similar interpretations. The simulation is done with phonon cutoff $[20, 40]$ for [tilt, rock] modes and $P_{\text{err}} \lesssim 10^{-11}$.

6.2.7 Discussion

The results of all configurations above share very similar properties and similar interpretations. In terms of spin-phonon coupling, as Ω_{eff} increases from 0.1 to $0.5\delta_{ah}$, level statistic $\langle r \rangle$ increases in an overall monotonous trend, deviating from the regime for integrable system ($\langle r \rangle \sim 0.39$). In Figure 13a, 16, 20a the spin imbalance $\langle L \rangle$ stays around its initial value of 2 for small Ω_{eff} but decays fast and stabilizes at a value close to 0 in the long term for large Ω_{eff} (see Figure 17a, 21a). When identical states are evolved under two slightly different Hamiltonians, difference between the spin observable $\Delta A_\psi(t)$ stays around 0 for small Ω_{eff} but deviates quickly to a larger value for large Ω_{eff} (see Figure 14a, 18a, 22a).

The evolution of $\Delta P_\psi(t)$ shows a consistent trend as it stays close to 1 for small Ω_{eff} but decays to 0 for large Ω_{eff} as shown in Figure 14b, 18b, 22b. Similar chaotic features are also demonstrated in [47]. Following the discussion in section 5, the three types signatures consistently indicates a significant evidence that the transition from normal to chaotic delocalization behavior in these systems is caused by strong spin-phonon coupling interactions.

The effect of the anharmonic phonon coupling is more complicated. Energy level statistics for one-drive configuration shows a clear monotonous decreasing trend as δ_{ah} increases. At $\delta_{ah} = 5\delta_0$ the anharmonic term is far off-resonance such that the effective coupling is negligible. With $\langle r \rangle \sim 0.39$ under this condition we expect the system to be integrable (see Figure 20). However, the behaviors probed using spin imbalance and slightly different Hamiltonians differ significantly from the case of small Ω . For instance, $\Delta L_\psi(t)$ quickly increases to a large value about 1 as compared to the resonant coupling case with a maximum deviation of $\Delta L_\psi(t) \sim 0.25$ (see Figure 22a and 23a). However $\Delta L_\psi(t)$ displays a quasi-periodic behavior that is also identified in the evolution of spin-imbalance observable (Figure 21b) and overlap (Figure 23b). Therefore, the contribution of anharmonic coupling to delocalization remain not clear. However it is likely

that anharmonicity affects the potential chaotic behavior in a different way than spin-phonon coupling. For further investigations, we will initialize the system with many similar initial states and average out their dynamics to see if the quasi-period structures can be erased. If such structures still exist, we can perform time series statistics such as Fourier or wavelet analysis to study their properties and origins. Otherwise, we might just arrive at the conclusion that anharmonicity does not have considerable contributions to delocalization in these systems. This seems to contradict the result of Ref. [25], where anharmonicity is a determining factor for delocalization. However, the model in Ref. [25] includes anharmonic coupling between multiple sets of modes and has a more complicated phonon Hamiltonian that is currently beyond the capability of our simulator. We are looking for innovative ways to solve this problem, such as introducing time-dependent trap confining frequencies.

Another crucial observation to make is that there exist inconsistencies between the chaotic signatures predicted by energy level statistics and those obtained using other methods. Besides the possibility of predicting the effects of anharmonicity as we just mentioned above, a larger $\langle r \rangle$ does not necessarily mean one quantum system has more chaotic behaviors than the other. For example, a two-drive three-site system with $\langle r \rangle \sim 0.51$ is not very different from a one-drive three-site system with $\langle r \rangle \sim 0.45$ in terms of other signatures. Further investigations are also required to elucidate the underlying reasons for these discrepancies.

7 Conclusion

In conclusion, this thesis has presented a comprehensive exploration of the mapping between photosynthesis-based spin-phonon models and a trapped-ion simulator. Based on the spin-only, spin-phonon, and harmonic/anharmonic phonon interactions that can be generated, we have proposed setups for three-ion prototype simulators to investigate vibration-environment assisted EET and anharmonicity induced quantum delocalization. We have generated preliminary results via numerical simulations to guide future experiments. Our EET results for donor-acceptor pairs involves transfer rate spectra with more complicated structures and they are in good consistency with results in the literature. Simulations for delocalization indicate that spin-phonon coupling is the primary factor leading to chaotic behavior, with the contribution of anharmonic coupling between different phonon modes remaining inconclusive and requiring further investigation. We have also identified potential inconsistencies between energy level statistics and other signatures of quantum chaos, which could be another intriguing direction for future research. Overall, results presented in this thesis provide a foundation for future experimental and theoretical investigations in atomic and many-body quantum physics.

8 Appendix

8.1 Appendix A

For detailed derivation of results in this section, see Appendix of [32].

1D Equilibrium Position

The total potential energy of a N-ion system is given by the sum of trap potential and Coulomb potential:

$$V_t = \frac{M}{2} \sum_{n=1}^N \sum_{i=1}^3 \omega_i^2 x_{ni}^2 + \frac{1}{2} \frac{Q^2}{4\pi\epsilon_0} \sum_{n \neq m}^N \left[\sum_{i=1}^3 (x_{ni} - x_{mi})^2 \right]^{-\frac{1}{2}}. \quad (8.1)$$

The equilibrium position along \hat{z} axis ($i = 3$) of the system is given by:

$$\frac{\partial V}{\partial x_{n3}} = 0. \quad (8.2)$$

It is convenient to define a dimensionless position variable u that is related to the real position by

$$u_n l_0 = x_{n3}, \quad l_0 = \left(\frac{Q^2}{4m\pi\epsilon_0\omega_z^2} \right)^{\frac{1}{3}}, \quad (8.3)$$

l_0 is the characteristic length scale of the system. The equilibrium position then be computed numerically by solving a system of N equations of u , the q th component of these equations is given by:

$$u_q + \sum_{m=q+1}^N \frac{1}{(u_m - u_q)^2} - \sum_{m=0}^{q-1} \frac{1}{(u_q - u_m)^2} = 0. \quad (8.4)$$

Tensors in Lagrangian The tensor A, C in Eq. (3.3), (3.6) are given by:

$$A_{mn} = \begin{cases} 1 + 2 \sum_{p=1, p \neq m}^N \frac{1}{|u_m - u_p|^3}, & m = n \\ \frac{-2}{|u_m - u_n|^3}, & m \neq n \end{cases} \quad (8.5)$$

$$C_{mnp} = \begin{cases} \sum_{q=1, q \neq m}^N \frac{\text{sgn}(q-m)}{(u_q - u_m)^4}, & m = n = p \\ \frac{-\text{sgn}(p-m)}{(u_p - u_m)^4}, & m = n \neq p = 0, m \neq n \neq p \end{cases} \quad (8.6)$$

8.2 Appendix B

Derivation of Hamiltonian in ordinary interaction frame

To obtain the spin part of \hat{H}_I (Eq. (3.28)), use identity of SU(2) transformation:

$$e^{-\frac{1}{2}i\hat{\theta}\hat{\sigma}} = \hat{I} \cos\left(\frac{\theta}{2}\right) - i\hat{\theta}\hat{\sigma} \sin\left(\frac{\theta}{2}\right). \quad (8.7)$$

$$\begin{aligned} \hat{U}^\dagger \hat{H}_{sI} \hat{U} &= \left[\hat{I} \cos\left(\frac{\omega_0 t}{2}\right) + i\hat{\sigma}_z \sin\left(\frac{\omega_0 t}{2}\right) \right] \hat{\sigma}_x \left[\hat{I} \cos\left(\frac{\omega_0 t}{2}\right) - i\hat{\sigma}_z \sin\left(\frac{\omega_0 t}{2}\right) \right] \\ &= \cos^2\left(\frac{\omega_0 t}{2}\right) \hat{\sigma}_x + i(\hat{\sigma}_z \hat{\sigma}_x - \hat{\sigma}_x \hat{\sigma}_z) \cos\left(\frac{\omega_0 t}{2}\right) \sin\left(\frac{\omega_0 t}{2}\right) + \hat{\sigma}_z \hat{\sigma}_x \hat{\sigma}_z \sin^2\left(\frac{\omega_0 t}{2}\right) \\ &= \cos(\omega_0 t) \hat{\sigma}_x - \sin(\omega_0 t) \hat{\sigma}_y \\ &= e^{i\omega_0 t} \hat{\sigma}^+ + e^{-i\omega_0 t} \hat{\sigma}^-. \end{aligned} \quad (8.8)$$

To obtain the phonon part, (Eq. (3.29)), consider the transformation for a specific phonon space m , use the identity in Appendix of [37]:

$$\exp[i\omega_m t \hat{b}_m^\dagger \hat{b}_m] \exp[ik(\hat{b}_m^\dagger + \hat{b}_m)] \exp[-i\omega_m t \hat{b}_m^\dagger \hat{b}_m] = \exp\left[ik\left(\hat{b}_m^\dagger e^{i\omega_m t} + \hat{b}_m e^{-i\omega_m t}\right)\right]. \quad (8.9)$$

which holds for some constant k . Therefore, neglecting the ion-index j , we have:

$$\begin{aligned} \hat{U}^\dagger \hat{H}_{mI} \hat{U} &= \frac{\Omega}{2} \exp \sum_m \left[i\zeta_m \left(\hat{b}_m^\dagger e^{i\omega_m t} + \hat{b}_m e^{-i\omega_m t} \right) \right] e^{-i(\omega_L t - \phi)} \\ &+ \frac{\Omega}{2} \exp \sum_m \left[-i\zeta_m \left(\hat{b}_m^\dagger e^{i\omega_m t} + \hat{b}_m e^{-i\omega_m t} \right) \right] e^{i(\omega_L t - \phi)}. \end{aligned} \quad (8.10)$$

in Lamb-Dicke Regime, we can expand the above Eq. to first order:

$$\exp \left[\pm \sum_m i\zeta_m \left(\hat{b}_m^\dagger e^{i\omega_m t} + \hat{b}_m e^{-i\omega_m t} \right) \right] = \hat{I} \pm \sum_m i\zeta_m \left(\hat{b}_m^\dagger e^{i\omega_m t} + \hat{b}_m e^{-i\omega_m t} \right), \quad (8.11)$$

$$\begin{aligned} \hat{U}^\dagger \hat{H}_{mI} \hat{U} &= \frac{\Omega}{2} \hat{I} \left[e^{-i(\omega_L t - \phi)} + e^{i(\omega_L t - \phi)} \right] \\ &+ \frac{\Omega}{2} \sum_m i\zeta_m \left(\hat{b}_m^\dagger e^{i\omega_m t} + \hat{b}_m e^{-i\omega_m t} \right) e^{-i(\omega_L t - \phi)} \\ &+ \frac{\Omega}{2} \sum_m -i\zeta_m \left(\hat{b}_m^\dagger e^{i\omega_m t} + \hat{b}_m e^{-i\omega_m t} \right) e^{i(\omega_L t - \phi)}. \end{aligned} \quad (8.12)$$

For derivation of (3.36), define phase constants:

$$\phi_m = \frac{1}{2}(\phi_b - \phi_r), \quad \phi_s = \frac{1}{2}(\phi_b + \phi_r + \pi), \quad (8.13)$$

and two operators:

$$\begin{aligned} \hat{A}_1 &= i(-\hat{\sigma}^- e^{-i\phi_b} + \hat{\sigma}^+ e^{i\phi_r}) = i(\hat{\sigma}^+ e^{i\phi_s} - \hat{\sigma}^- e^{-i\phi_s}) e^{-i\phi_m} = \hat{\sigma}^{\phi_s} e^{-i\phi_m}, \\ \hat{A}_2 &= i(\hat{\sigma}^+ e^{i\phi_b} - \hat{\sigma}^- e^{-i\phi_r}) = i(\hat{\sigma}^+ e^{i\phi_s} - \hat{\sigma}^- e^{-i\phi_s}) e^{i\phi_m} = \hat{\sigma}^{\phi_s} e^{i\phi_m}, \end{aligned} \quad (8.14)$$

$$\begin{aligned} \hat{H}'_I &= \hat{H}_r + \hat{H}_b \\ &= \frac{\Omega}{2} \sum_m \zeta_m \left[\hat{A}_1 \hat{b}_m e^{i\delta_m t} + \hat{A}_2 \hat{b}_m^\dagger e^{-i\delta_m t} + \hat{A}_1 \hat{b}_m^\dagger e^{i(\omega_m + \mu)t} + \hat{A}_2 \hat{b}_m e^{-i(\omega_m + \mu)t} \right] \\ &= \frac{\Omega}{2} \sum_m \zeta_m \hat{\sigma}^{\phi_s} \left[\hat{b}_m \left(e^{i(\delta_m t - \phi_m)} + e^{-i((\omega_m + \mu)t - \phi_m)} \right) + \hat{b}_m^\dagger \left(e^{-i(\delta_m t - \phi_m)} + e^{i((\omega_m + \mu)t - \phi_m)} \right) \right]. \end{aligned} \quad (8.15)$$

Since

$$e^{\mp i(\delta_m t - \phi_m)} + e^{\pm i((\omega_m + \mu)t - \phi_m)} = 2 \cos(\mu t - \phi_m) e^{\pm i\omega_m t}, \quad (8.16)$$

\hat{H}'_I can be further simplified to:

$$\hat{H}'_I = \Omega \sum_m \zeta_m \hat{\sigma}^{\phi_s} \cos(\mu t - \phi_m) (\hat{b}_m e^{-i\omega_m t} + \hat{b}_m^\dagger e^{i\omega_m t}). \quad (8.17)$$

For the transformation of anharmonic part, consider the transformation of generic axial/radial phonon operators $\hat{a}_p, \hat{b}_m^\dagger \hat{b}_n, \hat{b}_m^\dagger \hat{b}_n^\dagger$ acting on phonon space labeled by p, m, n under unitary operator $\hat{U} = \exp \left(-i \sum_q \nu_q t \hat{a}_q^\dagger \hat{a}_q \right)$, $\hat{U} = \exp \left(-i \sum_q \omega_q t \hat{b}_q^\dagger \hat{b}_q \right)$ where ν_q, ω_q are the axial/radial harmonic energy level spacing of mode q . For the transformation of \hat{a}_p ,

$$\begin{aligned} \hat{a}'_p &= \hat{U}^\dagger \hat{a}_p \hat{U} \\ &= \exp \left(i v_p \hat{a}_p^\dagger \hat{a}_p \right) \exp \left(i \sum_{p \neq q} \nu_q t \hat{a}_q^\dagger \hat{a}_q \right) \hat{a}_p \exp \left(-i \sum_{p \neq q} \nu_q t \hat{a}_q^\dagger \hat{a}_q \right) \exp \left(-i v_p t \hat{a}_p^\dagger \hat{a}_p \right). \end{aligned} \quad (8.18)$$

Using commutator properties

$$\left[\sum_{p \neq q} \nu \hat{a}_q^\dagger \hat{a}_q, \hat{a}_p \right] = 0 \quad [\hat{a}_p, \hat{a}_p^\dagger \hat{a}_p] = \hat{a}_p, \quad (8.19)$$

and Baker–Campbell–Hausdorff Formula [48],

$$e^{-\hat{B}} \hat{A} e^{\hat{B}} = \sum_n \frac{1}{n!} [\hat{A}, \hat{B}]^{\{n\}}, \quad (8.20)$$

$$\hat{a}'_p = \hat{a}_p \sum_n \frac{1}{n!} (-i\nu_p t)^n = e^{-i\nu_p t} \hat{a}_p. \quad (8.21)$$

Hence, \hat{a}_p picks up frequency $e^{-i\nu_p t}$ in this transformation. Then consider the transformation of $\hat{b}_m^\dagger \hat{b}_n$ which acts on some phonon spaces labeled by m, n under unitary operator $\hat{U} = \exp\left(-i \sum_q \omega_q t \hat{a}_q^\dagger \hat{a}_q\right)$, ω_q is the harmonic energy level spacing of space q . For $\hat{b}_m^\dagger \hat{b}_n$, if $m = n = k$, $\hat{b}_k^\dagger \hat{b}_k$ commutes with $\sum_q \omega_q \hat{b}_q^\dagger \hat{b}_q$ so it will remain unchanged after transformation. If $m \neq n$, $[\hat{b}_m^\dagger, \hat{b}_n] = 0$,

$$\begin{aligned} \hat{U}^\dagger \hat{b}_m^\dagger \hat{b}_n \hat{U} &= \exp\left(i\omega_n \hat{b}_n^\dagger \hat{b}_n\right) \exp\left(i\omega_m \hat{b}_m^\dagger \hat{b}_m\right) \exp\left(i \sum_{q \neq m, n} \omega_q \hat{b}_q^\dagger \hat{b}_q\right) \hat{b}_m^\dagger \hat{b}_n \exp\left(-i \sum_{q \neq m, n} \omega_q \hat{b}_q^\dagger \hat{b}_q\right) \exp\left(-i\omega_n \hat{b}_n^\dagger \hat{b}_n\right) \exp\left(-i\omega_m \hat{b}_m^\dagger \hat{b}_m\right) \\ &= \left[\exp\left(i\omega_n \hat{b}_n^\dagger \hat{b}_n\right) \hat{b}_n \exp\left(-i\omega_n \hat{b}_n^\dagger \hat{b}_n\right)\right] \left[\exp\left(i\omega_m \hat{b}_m^\dagger \hat{b}_m\right) \hat{b}_m^\dagger \exp\left(-i\omega_m \hat{b}_m^\dagger \hat{b}_m\right)\right] \\ &= e^{i(\omega_m - \omega_n)t} \hat{b}_m^\dagger \hat{b}_n, \end{aligned} \quad (8.22)$$

$\hat{b}_m^\dagger \hat{b}_n$ picks up $e^{i(\omega_m - \omega_n)t}$ (consistent with $m = n$ case). For $\hat{b}_m^\dagger \hat{b}_n^\dagger$, the case $m \neq n$ is just the same as the above where it picks up a factor $e^{i(\omega_m + \omega_n)t}$.

If $m = n = k$,

$$\begin{aligned} \hat{U}^\dagger \hat{b}_k^\dagger \hat{b}_k \hat{U} &= \exp\left(i\omega_k \hat{b}_k^\dagger \hat{b}_k\right) \exp\left(i \sum_{q \neq k} \omega_q \hat{b}_q^\dagger \hat{b}_q\right) \hat{b}_k^\dagger \hat{b}_k \exp\left(-i \sum_{q \neq k} \omega_q \hat{b}_q^\dagger \hat{b}_q\right) \exp\left(-i\omega_k \hat{b}_k^\dagger \hat{b}_k\right) \\ &= \exp\left(i\omega_k \hat{b}_k^\dagger \hat{b}_k\right) \hat{b}_k^\dagger \hat{b}_k \exp\left(-i\omega_k \hat{b}_k^\dagger \hat{b}_k\right) \\ &= e^{i2\omega_k t} \hat{b}_k^\dagger \hat{b}_k, \end{aligned} \quad (8.23)$$

where we have used again Baker–Campbell–Hausdorff and property $[\hat{b}_k^\dagger \hat{b}_k^\dagger, \hat{b}_k^\dagger \hat{b}_k] = -2\hat{b}_k^\dagger \hat{b}_k^\dagger$. Summarizing the derivations above, $\hat{a}_p \hat{b}_m^\dagger \hat{b}_n$ picks up a frequency Δ_{mnp}^- and $\hat{a}_p \hat{b}_m^\dagger \hat{b}_n^\dagger$ picks up Δ_{mnp}^+ .

$$\Delta_{mnp}^\pm = \omega_m \pm \omega_n - \nu_p. \quad (8.24)$$

Hence, equation (3.13) transforms to (3.37) in ordinary frame.

Derivation of Hamiltonian in resonant interaction frame

The Hamiltonian in resonant frame can be obtained in a similar way as the above derivations for ordinary frame. The difference between these two frames is caused by the change in unitary operator \hat{U} :

$$\begin{aligned} \sum_m \nu_m \hat{a}_m^\dagger \hat{a}_m &\rightarrow \mu_1 \left[\sum_m \hat{a}_m^\dagger \hat{a}_m \right], \\ \sum_m \omega_m \hat{b}_m^\dagger \hat{a}_m &\rightarrow \mu_2 \left[\sum_m \hat{b}_m^\dagger \hat{b}_m \right]. \end{aligned} \quad (8.25)$$

To derive the new form of Hamiltonian, we can do the substitution:

$$\nu_m \rightarrow \mu_1, \quad \omega_m \rightarrow \mu_2. \quad (8.26)$$

for all mode index m . Such a change of constant will not affect the validity of any step in the sector above.

Therefore, in equation (3.36) this substitution is equivalent to:

$$\delta_m \rightarrow 0, \quad \omega_m + \mu \rightarrow 2\mu. \quad (8.27)$$

which results in equation (4.5). For the anharmonic term, now $\hat{a}_p \hat{b}_m^\dagger \hat{b}_n$ picks up a frequency $\Delta'_{mnp} = -\mu_1$ and $\hat{a}_p \hat{b}_m^\dagger \hat{b}_n^\dagger$ picks up $\Delta'_{mnp} = 2\mu_2 - \mu_1$, resulting in Eq. (4.20).

8.3 Appendix C

8.3.1 Thermal state and average phonon number

Assuming phonon energy ω_0 and canonical ensemble with thermodynamics parameter $\beta = 1/K_b T$. The corresponding thermal state density matrix in fock basis is defined as

$$\hat{\rho}_{th} = \sum_n p_n |n\rangle \langle n|, \quad (8.28)$$

p_n is the probability of being in phonon eigenstate $|n\rangle$, neglecting the constant ground state energy ω_0 ,

$$p_n = \frac{1}{Z} e^{-\beta n \omega_0}, \quad (8.29)$$

$Z = \sum_{n=0}^{\infty} e^{-\beta n \omega_0}$ is the partition function. The average phonon number is given by:

$$\begin{aligned} \bar{n} &= \sum_n p_n n = -\frac{1}{\omega_0} \frac{\partial \ln Z}{\partial \beta} \\ &= \frac{1}{\exp(\beta \omega_0) - 1}. \end{aligned} \quad (8.30)$$

With given \bar{n} , β can be found inversely:

$$\beta = \frac{1}{\omega_0} \ln \left(\frac{1}{\bar{n}} + 1 \right). \quad (8.31)$$

The probability in equation (8.29) can be then rewritten in terms of \bar{n} :

$$p_n \propto e^{-\beta n \omega_0} = \left(\frac{1}{\bar{n}} + 1 \right)^{-n}. \quad (8.32)$$

Numerically we construct phonon state with a specified \bar{n} using (8.32) by initializing $\hat{\rho}_{th}$ with $\left(\frac{1}{\bar{n}} + 1 \right)^{-n}$ and normalize the trace to 1.

8.4 Appendix D

8.4.1 Relation between Decay rate and Dissipation in EET

We also tested the relation between near resonant transfer rate and dissipation. The result is shown in Figure 24

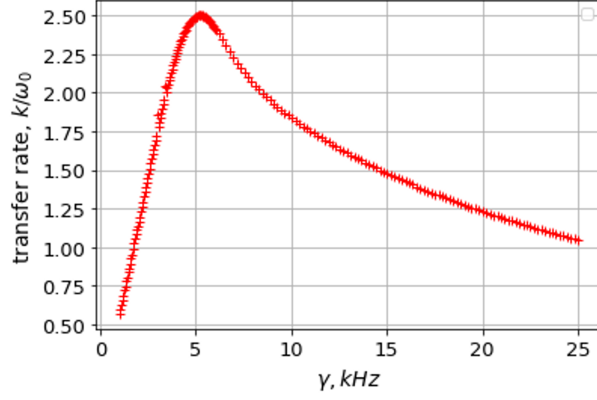


Figure 24: Normalized transfer ($\omega_0 = J_{12}$) rate as a function of effective cooling rate γ . Same parameters as in 2 are used with $\Delta E = 2\pi \times 100\text{kHz}$ ($n = 1$ resonance)

Qualitatively the result is consistent with [30]:

$$\begin{aligned}
 k &\propto \frac{1}{\gamma}, & \gamma > J \\
 k &\propto \gamma, & \gamma < J.
 \end{aligned} \tag{8.33}$$

References

- [1] Richard P Feynman. “Simulating physics with computers”. In: *Feynman and computation*. CRC Press, 2018, pp. 133–153.
- [2] Iulia M Georgescu, Sahel Ashhab, and Franco Nori. “Quantum simulation”. In: *Reviews of Modern Physics* 86.1 (2014), p. 153.
- [3] Markus Greiner et al. “Quantum phase transition from a superfluid to a Mott insulator in a gas of ultracold atoms”. In: *nature* 415.6867 (2002), pp. 39–44.
- [4] Christopher Monroe et al. “Programmable quantum simulations of spin systems with trapped ions”. In: *Reviews of Modern Physics* 93.2 (2021), p. 025001.
- [5] Ye Wang et al. “Single-qubit quantum memory exceeding ten-minute coherence time”. In: *Nature Photonics* 11.10 (2017), pp. 646–650. DOI: [10.1038/s41566-017-0007-1](https://doi.org/10.1038/s41566-017-0007-1). URL: <https://doi.org/10.1038/s41566-017-0007-1>.
- [6] Herbert Van Amerongen, Rienk Van Grondelle, et al. *Photosynthetic excitons*. World Scientific, 2000.
- [7] Yuan-Chung Cheng and Graham R Fleming. “Dynamics of light harvesting in photosynthesis”. In: *Annual review of physical chemistry* 60 (2009), pp. 241–262.
- [8] Ming-Jie Tao et al. “Coherent and incoherent theories for photosynthetic energy transfer”. In: *Science Bulletin* 65.4 (2020), pp. 318–328.
- [9] Andrei Tokmakoff. *Time-dependent quantum mechanics and spectroscopy*. Tech. rep. 2014.
- [10] Gregory D Scholes. “Long-range resonance energy transfer in molecular systems”. In: *Annual review of physical chemistry* 54.1 (2003), pp. 57–87.
- [11] Igor L Medintz and Niko Hildebrandt. *FRET-Forster Resonance Energy Transfer: From Theory to Applications*. John Wiley & Sons, 2013.
- [12] Volkhard May and Oliver Kühn. *Charge and energy transfer dynamics in molecular systems*. John Wiley & Sons, 2008.
- [13] Somayyeh Nemati, Carsten Henkel, and Janet Anders. “Coupling function from bath density of states”. In: *Europhysics Letters* 139.3 (2022), p. 36002.
- [14] Zhoufei Tang et al. “Extended hierarchy equation of motion for the spin-boson model”. In: *The Journal of Chemical Physics* 143.22 (2015), p. 224112.
- [15] Yu-Hsien Hwang-Fu, Wei Chen, and Yuan-Chung Cheng. “A coherent modified Redfield theory for excitation energy transfer in molecular aggregates”. In: *Chemical Physics* 447 (2015), pp. 46–53.
- [16] Filippo Caruso et al. “Highly efficient energy excitation transfer in light-harvesting complexes: The fundamental role of noise-assisted transport”. In: *The Journal of Chemical Physics* 131.10 (2009), 09B612.
- [17] Gregory S Engel et al. “Evidence for wavelike energy transfer through quantum coherence in photosynthetic systems”. In: *Nature* 446.7137 (2007), pp. 782–786.
- [18] EK Irish, R Gómez-Bombarelli, and BW Lovett. “Vibration-assisted resonance in photosynthetic excitation-energy transfer”. In: *Physical Review A* 90.1 (2014), p. 012510.
- [19] Hao Chen et al. “Phonon-mediated excitation energy transfer in a detuned multi-sites system”. In: *Journal of Physics B: Atomic, Molecular and Optical Physics* 52.7 (2019), p. 075501.

- [20] Francesca Fassioli and Alexandra Olaya-Castro. “Distribution of entanglement in light-harvesting complexes and their quantum efficiency”. In: *New Journal of Physics* 12.8 (2010), p. 085006.
- [21] Ethan Wyke, Abuenamleh Aiyejina, and Roger Andrews. “Quantum excitation transfer, entanglement, and coherence in a trimer of two-level systems at finite temperature”. In: *Physical Review A* 101.6 (2020), p. 062101.
- [22] Rahul Nandkishore and David A Huse. “Many-body localization and thermalization in quantum statistical mechanics”. In: *Annu. Rev. Condens. Matter Phys.* 6.1 (2015), pp. 15–38.
- [23] Eric J Heller. “Mode mixing and chaos induced by potential surface crossings”. In: *The Journal of chemical physics* 92.3 (1990), pp. 1718–1727.
- [24] Sourav Karmakar and Srihari Keshavamurthy. “Intramolecular vibrational energy redistribution and the quantum ergodicity transition: a phase space perspective”. In: *Physical Chemistry Chemical Physics* 22.20 (2020), pp. 11139–11173.
- [25] Chenghao Zhang et al. “Surface crossing and energy flow in many-dimensional quantum systems”. In: *Proceedings of the National Academy of Sciences* 120.9 (2023), e2221690120.
- [26] FL Semião, K Furuya, and GJ Milburn. “Vibration-enhanced quantum transport”. In: *New Journal of Physics* 12.8 (2010), p. 083033.
- [27] I Wilson-Rae, P Zoller, and A Imamoglu. “Laser cooling of a nanomechanical resonator mode to its quantum ground state”. In: *Physical Review Letters* 92.7 (2004), p. 075507.
- [28] Daniel Barredo et al. “Coherent excitation transfer in a spin chain of three Rydberg atoms”. In: *Physical review letters* 114.11 (2015), p. 113002.
- [29] Nils Trautmann and Philipp Hauke. “Trapped-ion quantum simulation of excitation transport: Disordered, noisy, and long-range connected quantum networks”. In: *Physical Review A* 97.2 (2018), p. 023606.
- [30] Frank Schlawin et al. “Continuously parametrized quantum simulation of molecular electron-transfer reactions”. In: *PRX Quantum* 2.1 (2021), p. 010314.
- [31] Daniel A Steck. “Quantum and atom optics”. In: (2007).
- [32] Cyrille Marquet, Ferdinand Schmidt-Kaler, and Daniel FV James. “Phonon–phonon interactions due to non-linear effects in a linear ion trap”. In: *Applied Physics B* 76 (2003), pp. 199–208.
- [33] Kazi Rajibul Islam. *Quantum simulation of interacting spin models with trapped ions*. University of Maryland, College Park, 2012.
- [34] Dietrich Leibfried et al. “Quantum dynamics of single trapped ions”. In: *Reviews of Modern Physics* 75.1 (2003), p. 281.
- [35] Lev Davidovich Landau, Evgenii Mikhailovich Lifshits, and Evgenij Mihajlovic Lifsic. *Mechanics*. Vol. 1. CUP Archive, 1960.
- [36] Marco Frasca. “A modern review of the two-level approximation”. In: *Annals of Physics* 306.2 (2003), pp. 193–208.
- [37] Ch Schneider, Diego Porras, and Tobias Schaetz. “Experimental quantum simulations of many-body physics with trapped ions”. In: *Reports on Progress in Physics* 75.2 (2012), p. 024401.
- [38] Aaron Christopher Lee. “Engineering a quantum many-body hamiltonian with trapped ions”. PhD thesis. University of Maryland, College Park, 2016.

- [39] DJ Larson et al. “Sympathetic cooling of trapped ions: A laser-cooled two-species nonneutral ion plasma”. In: *Physical review letters* 57.1 (1986), p. 70.
- [40] Shiqian Ding et al. “Quantum simulation with a trilinear hamiltonian”. In: *Physical Review Letters* 121.13 (2018), p. 130502.
- [41] J Robert Johansson, Paul D Nation, and Franco Nori. “QuTiP: An open-source Python framework for the dynamics of open quantum systems”. In: *Computer Physics Communications* 183.8 (2012), pp. 1760–1772.
- [42] Daniel Manzano. “A short introduction to the Lindblad master equation”. In: *Aip Advances* 10.2 (2020), p. 025106.
- [43] Ernst Hairer, Syvert P Nørsett, and Gerhard Wanner. *Solving ordinary differential equations. 1, Nonstiff problems*. Springer-Vlg, 1993.
- [44] Herbert Goldstein. *Classical mechanics*. Pearson Education India, 2011.
- [45] Fritz Haake. *Quantum signatures of chaos*. Springer, 1991.
- [46] William Morong et al. “Observation of Stark many-body localization without disorder”. In: *Nature* 599.7885 (2021), pp. 393–398.
- [47] Eric Boyers et al. “Exploring 2D synthetic quantum Hall physics with a quasiperiodically driven qubit”. In: *Physical Review Letters* 125.16 (2020), p. 160505.
- [48] Jun John Sakurai and Eugene D Commins. *Modern quantum mechanics, revised edition*. 1995.